A PULSED LASER LOADING TECHNIQUE FOR CONTROLLED DYNAMIC LOADING OF NANOSTRUCTURED MATERIALS

BY

OWEN THOMAS KINGSTEDT

THESIS

Submitted in partial fulfillment of the requirements
for the degree of Master of Science in Aerospace Engineering
in the Graduate College of the
University of Illinois at Urbana-Champaign, 2011

Urbana, Illinois

Adviser:

Professor John Lambros

Abstract

This thesis presents an improved laser loading technique for controlling and calibrating the stress waves created from this ultra-high loading rate technique. In the high-power pulsed laser loading technique, a laser produced compressive stress pulse passes through a substrate and reflects at a traction free surface as a tensile wave of opposite sign and direction. During the reflection process the traction free surface moves out-of-plane, allowing for measurement of surface displacement that can be related to the stress wave profile through the use of one-dimensional wave mechanics. In this work we improved upon this traditional pulsed laser loading technique by adding a set of optical components that can control the laser power deposited onto the sample down to 2% (of full power) increments. We also performed parametric studies that precisely quantified the resulting laser loading pulse based on experimental parameters such as the energy absorbing and the confining layer thicknesses. (Both these parameters are aspects of the layered substrate sample used to generate the stress wave.) Through the testing of precisely manufactured calibration samples with aluminum energy absorbing layers of 500 nm and waterglass confining layers of 7.62 μm, which were found to be the best combinations of these thicknesses, stress wave profiles are obtained over a nearly continuous laser energy spectrum at the 2% power increments. Repeatable stress wave profiles showing consistent rise times and decay times were obtained at the selected energy levels. The stress wave profile peaks that were measured ranged from 1101.3 MPa ± 270 MPa to 1731.3 MPa ±237 MPa, as the laser power varied from 30% to 50% of peak. Below 30% laser power no analyzable signal was obtained, and above 50% power the Si substrates failed at every loading. With the improved methodology developed in this work it will be possible to employ the laser

loading power as a calibration for the resulting stress wave in each case, and therefore use calibrated curves as input to numerical simulations.

To those that spend late nights toiling

over the sciences hoping to better the world we live in.

Acknowledgements

The work presented in this thesis would not have been possible without the support of many people. The work conducted in this thesis was supported by DOE grant DEFG52-09NA29463. Most importantly the author wishes to thank his adviser, Prof. J. Lambros of the Department of Aerospace Engineering, whose guidance, patience and encouragement have been irreplaceable resources during the course of this research. Many thanks to Prof. I. Robertson and Prof P. Sofronis whose input was valuable in the development of the results presented.

The author thanks the Fredrick Seitz Materials Research staff Steve Burdin and Bharat Sankaran, for help on training on various MRL instruments and the Micro-Nano-Mechanical Systems cleanroom staff members Dr. Glennys Mensing and Michael Hansen for their thought provoking discussions and assistance on microfabrication techniques.

Table of Contents

List of Figures

List of Tables:

Chapter 1: Introduction

1.1 Prior Research

Shortly after the invention of the laser in 1958, White (1963) examined the elastic waves created in a solid by the thermal expansion of the material when it was loaded by a transient heating source, such as a short-duration high-power laser pulse. Such lasers are an attractive heating source because of their ability to expose a material surface to large amounts of energy over a very short time. If the laser pulse energy is large enough, the exposed material is ablated, causing a rapid volumetric expansion which launches a compressive loading pulse through the material. Once the compressive pulse travels through the material to the back side of the material, the pulse reflects at the free surface as a tensile wave, loading the material in tension. Skeen and York (1968) were the first to study the magnitude of stress waves created when different materials were subjected to high levels of laser energy, 60J over 60 ns. Skeen mounted samples onto simple pendulums and monitored the displacement of the pendulum using strobe imaging, to determine the magnitude of the stress wave created. Using this method Skeen was able to produce impulses in aluminum on the order of 2.4 GPa.

Anderholm (1970) looked to improve the level of stress that could be created with lower powered lasers, 7J over 12 ns, in a materials when using the laser loading technique by first depositing a thin layer of aluminum on the material surface to act as a laser "energy absorbing" layer, and adding a transparent "confining layer" on top of the energy absorbing layer. Anderholm (1970) was able to created shock waves in aluminum of 3.4 GPa in magnitude with a duration on the order of nanoseconds. The addition of the thin energy absorbing film and the

confining layer demonstrated the desired effect of being able to produce stress waves of gigapascal magnitude with the use of less powerful lasers.

The laser loading method was further developed by Yuan and Gupta (1993). Yuan and Gupta were the first to incorporate the use of interferometry on the non-loading side of a sample to directly measure the propagating stress wave profile. Furthermore Yuan and Gupta (1993) examined the effects of various absorbing layers, confining layers, and substrates on the temporal shape of the stress pulse. From their work three important conclusions were reached: (1) Solid confining layers are needed to produce high amplitude, low rise time stress wave pulses, verifying Anderholm's (1970) results. Solid waterglass was found to be the optimal material for this application. (2) Vapor deposited aluminum is the most promising material to use as the energy absorbing layer because of its relatively low cost, ease of deposition, and its high thermal expansion, allowing it to easily convert laser energy to mechanical energy. (3) The shape of the stress pulse is dependent on the type of substrate material selected.

After the early studies of White (1963), Skeen and York (1968), and Anderholm (1970), who focused on the interaction of the laser with a single material layer, the laser loading technique has been used in the experimental study of transient events in thin films and small scale structures. Laser loading is especially well suited for this role, which has become more prevalent with the increased interest in micro- and nano-mechanics over recent decades, because it is rapid enough to cause significant inertial loading in structures with small mass which at lower loading rates may not exhibit dynamic effects. Gupta and Argon (1990) devised a laser loading based set-up for quantifying the spallation strength of thin films, on the order of 10 μm. In the laser spallation technique, a laser pulse is directed at a substrate with the intent to cause thin films deposited on the substrate to fail in tension, hence spalling from the surface. A laser

spallation specimen is shown in Figure 1.1. During a laser spallation test, the released laser energy ablates the energy absorbing layer causing a rapid volumetric expansion which is constrained by a solid confining layer, launching a compression stress wave through the substrate propagating towards the thin films on the non-loading side of the sample. At the non-loading side the compressive stress wave reflects as tension. If the amplitude of the reflected tensile wave is greater than the adhesion strength of the thin film to the substrate, the thin film is spalled from the substrate surface (Pronin and Gupta, 1998).

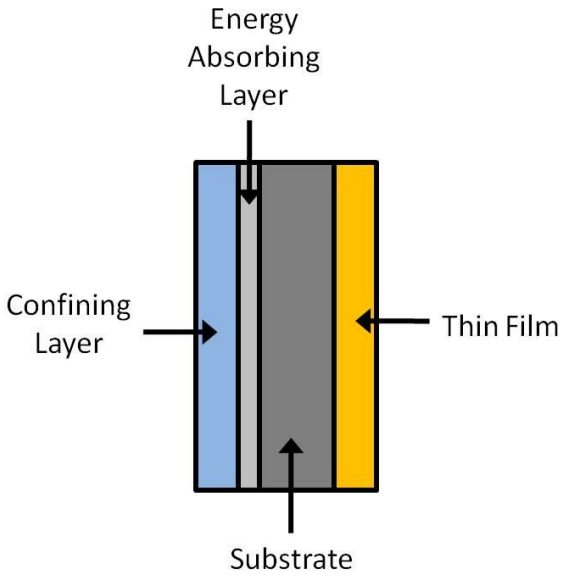

Figure 1.1: Laser spallation sample

Subsequently, others have used a similar method to examine spallation strength of materials via the laser loading (Gupta *et al.*, 1992, 1993; Wang *et al* ., 2002, 2004; Kandula, 2008).

Kimberly *et al.* (2008) applied the laser loading method to study small scale devices, namely Microelectricalmechanical Systems (MEMS). In their effort the same type of laser loading approach illustrated in Figure 1.1 was used, but instead of loading a thin film, patterned microdevices were situated on the free surface. Their investigation into the response of MEMS

systems to severe dynamic loading was able to show that different failure modes can occur in MEMS devices depending on device geometry and loading rate.

In situations in which a single thin film is being investigated, measuring the out-of-plane motion of the film, as first done by Yuan and Gupta (1993), can yield the stress at the film-substrate interface. If more complicated devices are patterned on the substrate, as in the work of Kimbeley *et al.* (2008), the single point out-of-plane displacement measurement is not characteristic of the entire structure, since the device geometry is complex. Therefore, in that work a finite element simulation was used to find local stresses obtained by using the single point displacement measurement as the loading input.

In the future, we would like to extend the efforts of thin films to the study of the strengthening effect present in nanolayered metals. Work conducted by Misra *et al.* (2005), see Figure 1.2, was able to show that as the layer thickness decreases from micron to nanometer thickness there is a strengthening effect seen on the bulk material. Using the laser loading approach we would like to probe multilayered materials over decreasing layering thicknesses and to examine the deformation induced by the laser loading. However, the understanding of such multilayer systems will necessitate companion numerical simulations that will need precise loading conditions as input. The objective of this work, described in more detail below, is to obtain such information accurately and repeatably.

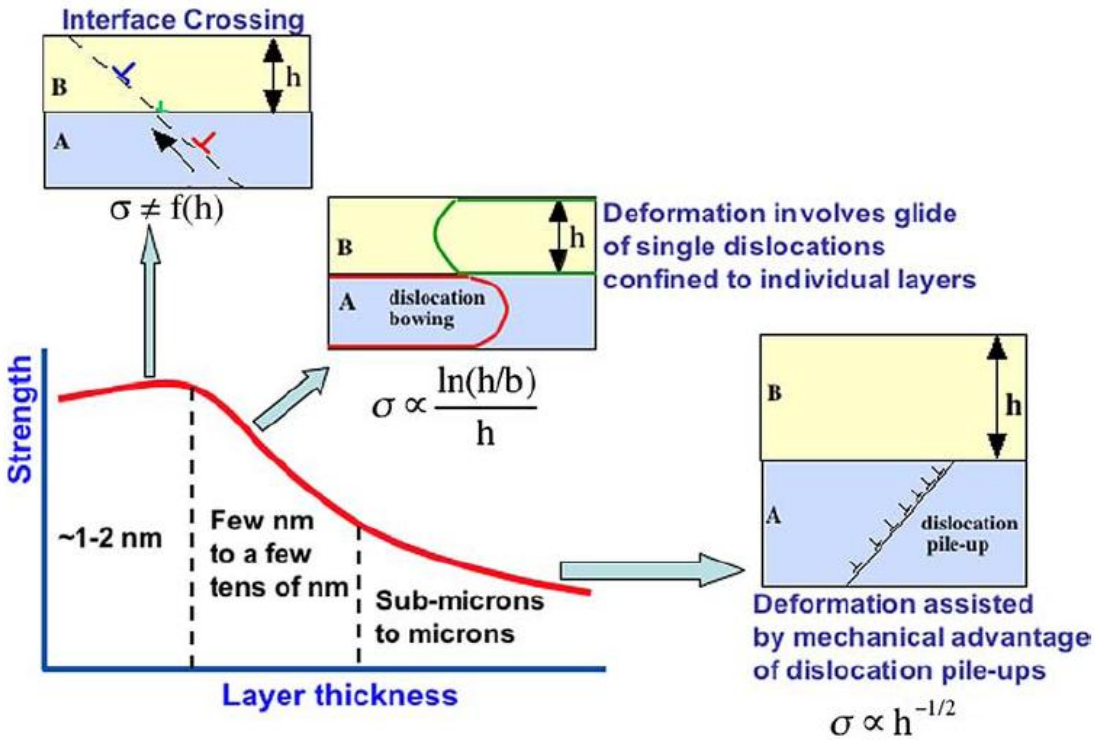

Figure 1.2: Effect of layer thickness on bulk material strength. Misra *et al.* (2005)

1.2 Objectives and Approach

The ultimate objective of this work is to experimentally obtain a consistent stress pulse created using the laser loading method at varying levels of laser energy intensity and have a quantitative prediction of what the pulse would be. Previous work by Yuan and Gupta (1993) has examined the effect of laser energy level, but the study was conducted at three laser energy magnitudes with significant separation among them. The aim of this work is to improve upon their study by *probing laser energy levels over a continuous spectrum of laser power*. To conduct this more refined study of the stress wave profile at varying energy levels it is first necessary to create well controlled calibration specimens. Development of the calibration

specimens requires careful fabrication and characterization of manufactured specimens. Once a well defined calibration specimen is developed, it will be subjected to laser loading with the interferometric diagnostics to monitor the out-of-plane displacement of the specimen traction free surface. The recorded interferometer data will be analyzed to obtain a temporal stress wave profile to demonstrate that the developed calibration specimens and laser loading technique are able to produce a repeatable propagating stress wave. This work is of great importance because the results obtained here can subsequently be used as input for validation of computational models of multilayered geometries where well characterized inputs are required.

1.3 Outline

Chapter 2 of this thesis describes the laser loading experimental method in detail as well as the data analysis methods used in this particular work. The experimental set-up used here is an improvement over that previously used by Kimberley *et al.* (2008). The improvements made to the set-up have led to a reduction in ambient noise in the recorded data, an increased range of sample geometries that can be tested, and a greatly increased level of control over the amount of laser energy imparted in the samples.

The development of the calibration specimens used for this study is discussed in chapter 3. The necessary metallic depositions and their characterizations are explained in detail. A study of the waterglass application process and the effects of the spin coating speed on the final waterglass thickness is presented. In chapter 4 the experimentally obtained stress wave profiles obtained from the laser loading method are presented. The stress wave profiles were obtained for eight different laser energy levels, ranging between 30 % and 50% of the maximum laser

energy. The average stress wave profile is calculated for each of the laser energy levels, and is accompanied by an analysis of the stress wave rise and decay.

Finally, chapter 5 presents the conclusions obtained from this study and future considerations for the work presented. From this study repeatable stress wave profiles were obtained for each of the laser energy levels tested. The success of this study lends itself for use in many future applications; three of particular interest are discussed at the end of this work.

Chapter 2: Experimental Method

2.1 Elementary Theory

The analyses techniques used in this experimental effort are based on one dimensional uniaxial strain wave propagation theory. Additionally, an understanding of this simple wave propagation framework can aid in interpreting the physical processes present. A particular case of uniaxial wave propagation of interest here is the reflection of a stress wave at a traction free surface. The reflection process of a stress wave is shown in detail in the schematics of Figure 2.1. In Figure 2.1 (a), an elastic compression wave, shown with an idealized Gaussian distribution spatial profile and illustrated as positive, moves through a material to the right towards a traction free surface. The material vertical dimension is considered to be much greater than the lateral one resulting in uniaxial strain conditions prevailing in the material, and consequently a wave speed of $c_d = \sqrt{(\lambda + 2\mu)/\rho}$, where λ and μ are the material Lamé constants, and ρ is the material density. The reflection process begins in the schematic shown in Figure 2.1 (b) with a small portion of the incident (σ_I) wave having reflected as a tensile wave (σ_R) now shown below the x-axis, of the same profile as the incident compression wave. Half way through the reflection process, the time instant seen in Figure 2.1 (c), the profiles and magnitudes of the incident and reflected waves are equal and opposite. Therefore, at this instant the compressive and tensile stress waves cancel each other out exactly, leading to zero stress in the material. The velocity of the material particles in this region is twice that of the incident wave (Kolsky, 1953). As the reflection process continues beyond this region of cancelation, the stress state in the material becomes tensile. As shown in Figure 2.1 (d) the reflected tensile wave is of the same profile as the incident wave, and magnitude, but opposite in propagation direction and sign. In Figure 2.1

(d) the dashed line represents the *first* plane in the material that experiences the maximum tensile stress during the reflection process. If this tensile stress induced by the reflecting stress wave is equal to or greater, than the tensile strength of the material (which often is less than the compressive strength) spallation will occur on this plane causing the portion of the specimen to the right of the dashed line to tear away from the material, as shown in Figure 2.1 (e). Note that the portion of the specimen that is removed from the substrate moves to the right, and that the stress wave in the material is dissipated by the spallation of material.

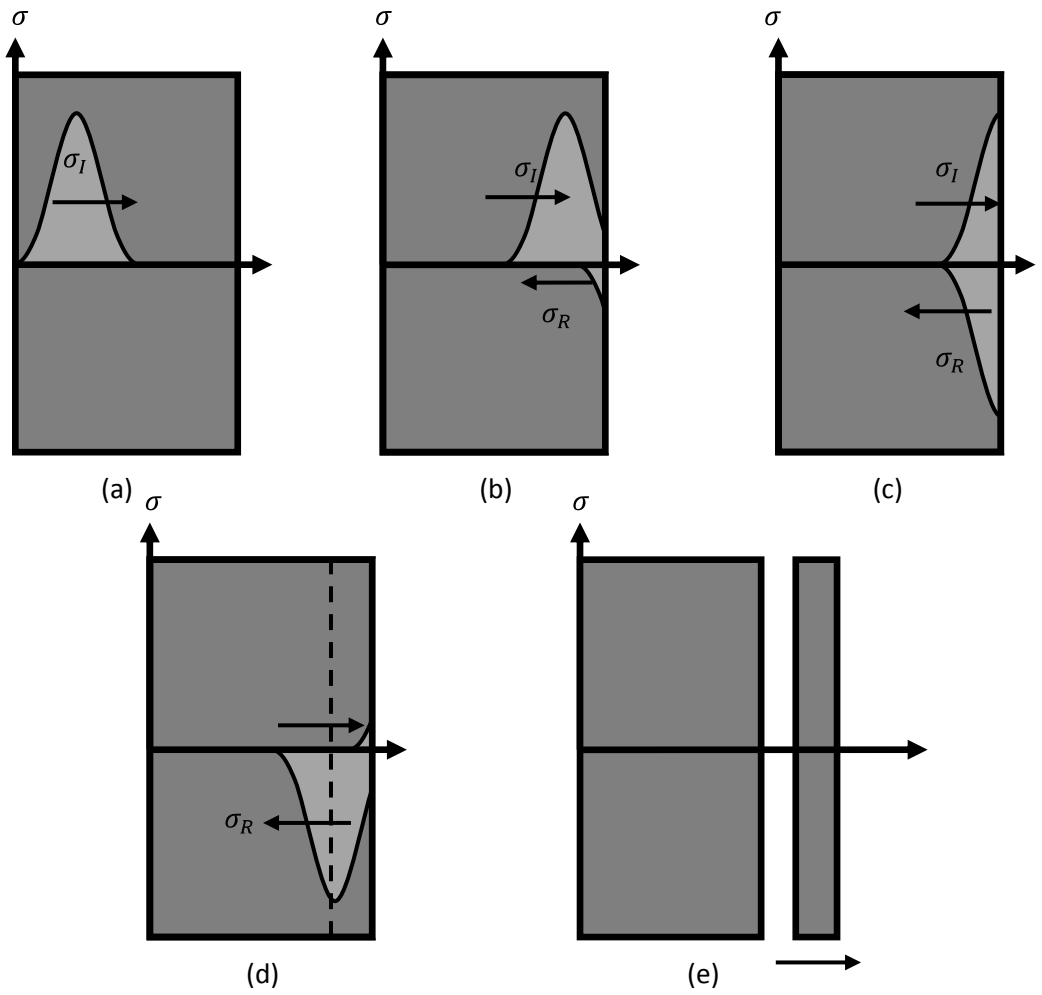

Figure 2.1: Schematic of the reflection process of a stress wave at a free surface and the spallation process. (a) An incident compressive stress wave (σ_I) travels to the right through a material towards a free surface. (b) The reflection process begins with a portion of the stress wave reflecting (σ_R) at the free surface as a tensile wave towards the left with the same profile as the incident wave. (c) Half way through the reflection process, the incident and reflected waves cancel, causing a region of zero stress. (d) The reflection process continues and the material is in tensile state. The dashed like represents the plane in the material that is exposed to a tensile stress greater than the tensile strength of the material. (e) Spallation occurs on the plane represented by the dashed line in (d). A portion of the material is torn from the material and travels to the right dissipating the stress wave within the material.

In addition to this physical understanding of the reflection process and associated spallation, uniaxial strain wave propagation theory can be used to quantify the stress pulse

traveling in the material. The magnitude of the stress wave passing through a solid can be determined if the free surface velocity is known during the reflection process. Assuming one dimensional wave propagation, the stress in the substrate is related to the free surface velocity through

$$\sigma_I(t) = \frac{1}{2}\rho c_d \frac{\partial u(t)}{\partial t} \quad , \tag{2.1}$$

where $\sigma_I(t)$ is the variation of the magnitude of incident stress with time, ρ is the density of the substrate, c_d is the dilatational wave speed of the substrate, and $\partial u(t)/\partial t$ is the velocity of free surface in time (Zukas, 1982). Thus, measurement of the free surface velocity at a single point on the free surface suffices to measure the temporal stress profile of the travelling wave, at least for the duration over which uniaxial conditions prevail, namely the time it takes form stress waves form the later boundaries to reach the measurement location.

2.2 Experimental Set-up

The laser loading experimental setup used for the present work was originally used in the study of the dynamic failure of Microelectromechanical Systems (MEMS) devices and thin films (Kimberley, 2008). In that work the MEMS structures were small enough that the substrate stress could still be measured at locations away from the structures. However in our future efforts which will concentrate on blanket thin films this will not be the case. Therefore precise knowledge, and control, of the stress pulse travelling in a single silicon substrate is necessary. As a result several improvements were made to the set up of Kimberley *et al.* (2008), namely: (1) a set of three optics (beam splitting polarizer, half wave plate and glass wedge) where added to provided a means of controlling the amount of laser energy the samples are exposed to, (2) a new

sample holder was created to allow for a larger variety of sample dimensions to be tested, (3) additional translation stages were added to provide more consistent alignment of the Michelson interferometer that measures free surface velocity, and (4) the set up was mounted on an air isolated optical table to reduce the effects of ambient vibrations on the recorded data. The improved experimental set-up used for the work presented here is schematically displayed in Figure 2.2, a photograph of it is shown in Figure 2.3.

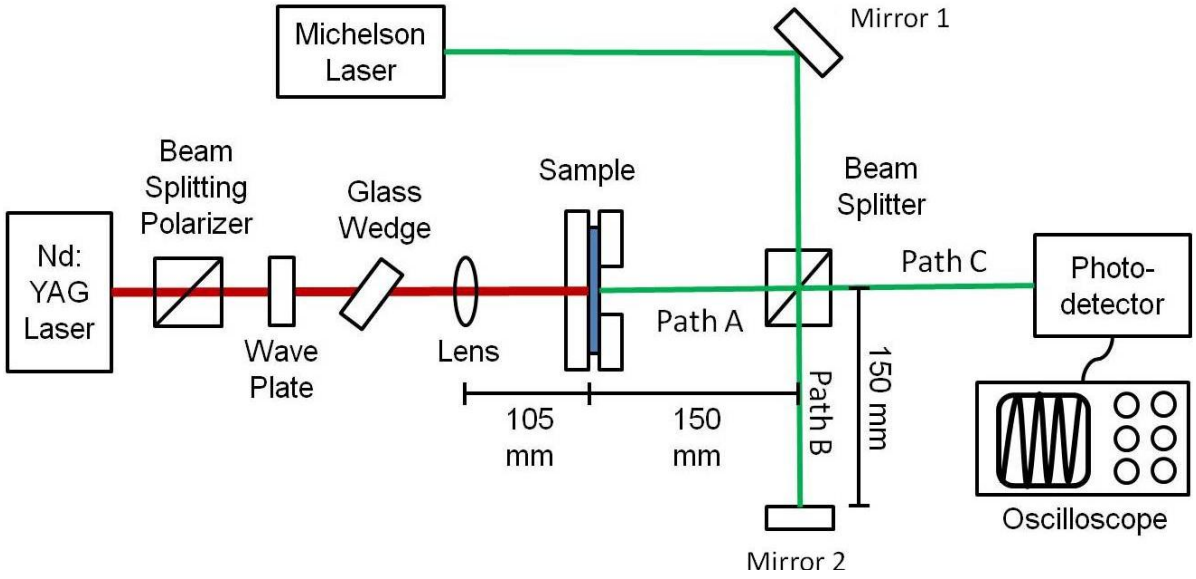

Figure 2.2: A schematic of the laser loading test setup (red path), with Michelson interferometer (green path).

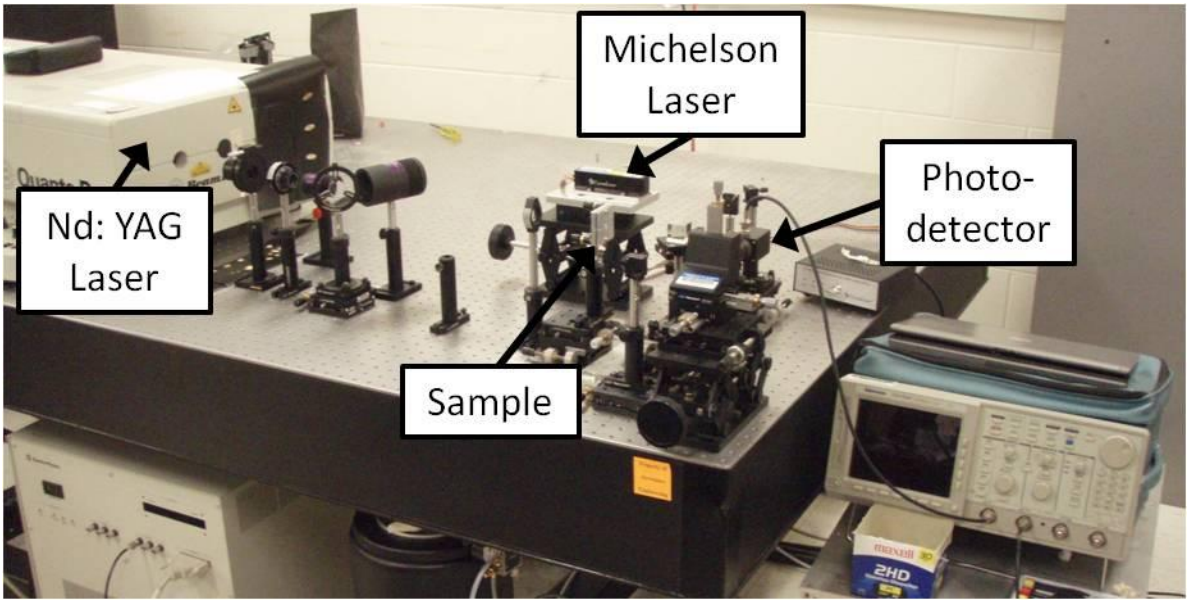

Figure 2.3: A photograph of the laser loading test setup.

Stress waves in the specimens are produced through the use of a Neodymium-doped Yttrium Aluminum Garnet (Nd:YAG) laser. The Nd:YAG laser used produces an infrared (IR) pulse 8-12 ns in duration at a wavelength of 1064 nm. The laser produces a nominal spot size of 10 mm diameter with a top hat cross sectional profile, in accordance with manufacturer specifications. The laser pulse first passes through a beam splitting polarizer, which resolves the IR light wave that passes through into two mutually perpendicular components. The component of the light wave that is parallel to the axis of polarization is transmitted, while the component perpendicular to the axis of polarization is rejected by the polarizer (Dally, 2005). When the polarization axis of the Nd:YAG laser is coincident with the polarization axis of the beam splitting polarizer 100% of the laser pulse is transmitted. When the polarization axis of the laser is perpendicular to the polarization axis of the beam splitting polarizer 0% of the laser pulse is transmitted. After passing through the beam splitting polarizer, the pulse passes through a half wave plate. The half wave plate resolves the laser light wave into two orthogonal components

and transmits the components with different velocities, a fast axis and a slow axis, creating circularly polarized light. The circularly polarized light passes through a glass wedge placed at Brewster's angle, *i.e.*, the angle of incidence at which light with a particular polarization is perfectly transmitted through a glass surface with no reflection. Based on the angle of the beam splitting polarizer, and the angle of the half wave plate the polarization of the circularly polarized light that reaches the glass wedge can have different directions, which could be reflected or transmitted.

A study of incremental angles of the beam splitting polarizer and the half wave plate with the glass wedge in place was conducted to precisely determine the laser power that passes through this optical arrangement. The results of this study can be seen in Figure 2.4 as a variation of normalized peak laser energy (with the maximum being 100%) versus wave plate angle for different orientations of the polarizer . From Figure 2.4 it can be seen that through the use of this optical arrangement the amount of laser energy that specimens can be subjected to can be finely controlled in increments of as little as 2% of the maximum laser energy. In addition, the nominal laser spot size of 10 mm can be reduced to 3 mm diameter though a plano-convex lens with a focal length of 150 mm, placed after the glass wedge as seen in Figure 2.2. The focusing lens is used to vary the level of fluence of the laser pulse. Fluence is a measure of laser energy over area, typically expressed in J/cm^2. For a 3 mm diameter spot size the fluence of a laser pulse in this set up at maximum power is 67.70 J/cm^2, while for a 10 mm spot it is 6.09 J/cm^2.

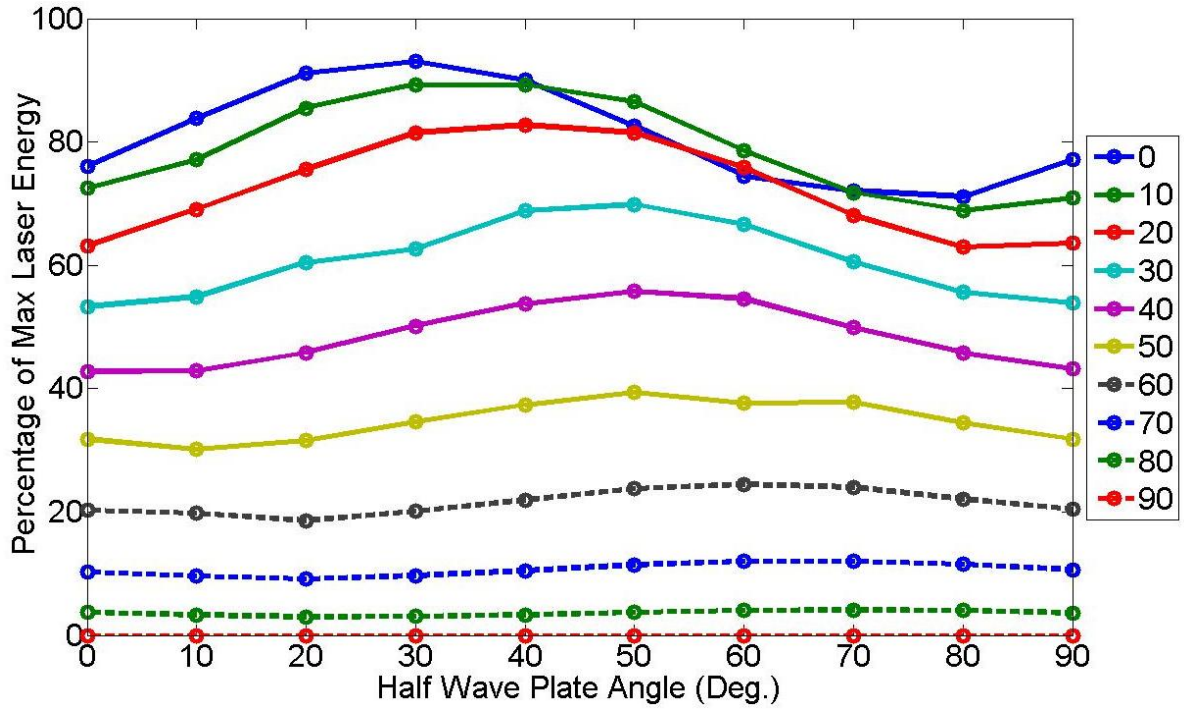

Figure 2.4: The normalized laser energy measured for each beam splitting polarizer angle between 0 and 90 degrees is plotted against the angle of the half wave plate. A sample can be subjected to energy levels between 0% and 93% of the maximum laser energy. Losses within the optics prevent subjecting samples to 100% of the laser energy.

The specimens are held in a compression holder, schematically displayed in Figure 2.5, and are placed in the path of the laser as shown in Figure 2.2. Unlike that used in Kimberley *et al*. (2008), the sample holder was designed to allow for testing specimens of different sizes and shapes. The samples tested here, described in more detail in chapter 3, are 12 mm by 12 mm squares, consisting of a confining layer and energy absorbing layer on the loading side of the sample, and a reflective layer on the non-loading side of the sample, as seen in Figure 2.6. Once placed in the holder, four screws are tightened until the sample is held firmly in compression, to prevent sample movement within the holder. The holder has been designed to allow future testing of other samples that are either 5 mm x 5mm square, or circular samples of 5 mm or 10 mm diameter.

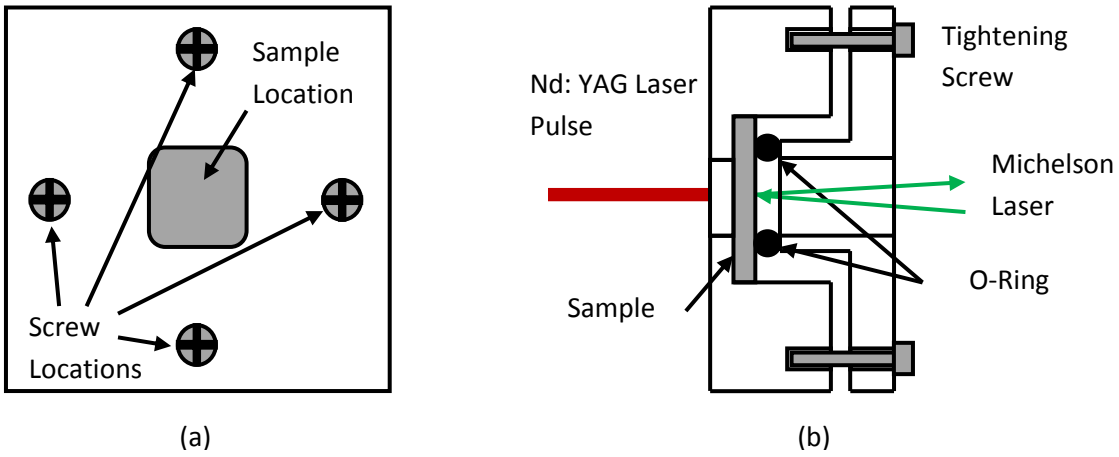

Figure 2.5: Laser loading compression specimen holder. (a) A front view of the holder, the laser loading side. (b) Cross section view of the holder.

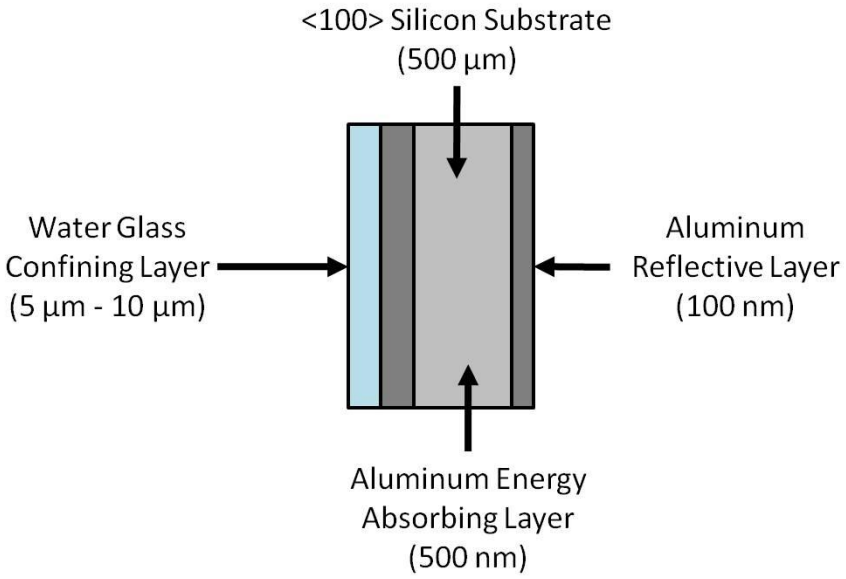

Figure 2.6: Side view of a typical specimen lay up

As in Wang *et al*. (2004) and Kimberley (2008), to capture the out-of-plane motion of the free surface of the specimen (opposite the loading side), a Michelson interferometer is utilized on the back side (non-loading side) of the specimen. A diode pumped solid state laser (CrystaLaser CW Green Laser) of 532 nm wavelength is used in the interferometer because it produces a highly stable beam intensity which is necessary for Michelson interferometry. As illustrated in

Figure 2.2, the Michelson laser is reflected from stationary mirror 1 though a beam splitter. The beam splitter directs half of the Michelson laser energy at stationary mirror two, and the remaining half at the specimen. Stationary mirror 2 reflects the laser energy back into the beam splitter and into a photodetector. The reflective layer on the back side of the sample sends the laser energy back through the beam splitter and into the photodetector. The photodetector measures the energy intensity of the light exposed to the active area, and outputs the intensity history to a high speed (3 GS/s) digitizing oscilloscope (Tektronix 684C). The Michelson interferometer relies on the interference of the Michelson laser light to measure the out-of-plane displacement of the traction free surface of the specimen. Prior to specimen loading, path A and path B are equal in length, nominally 150 mm. As the stress wave created by the Nd:YAG laser reflects at the free surface of the specimen, as described in section 2.1, the out-of-plane displacement of the sample free surface causes changes to the length of path B, thus producing constructive and destructive interference of the laser light in path C. Figure 2.7 shows a typical light intensity data signal as recorded by the oscilloscope.

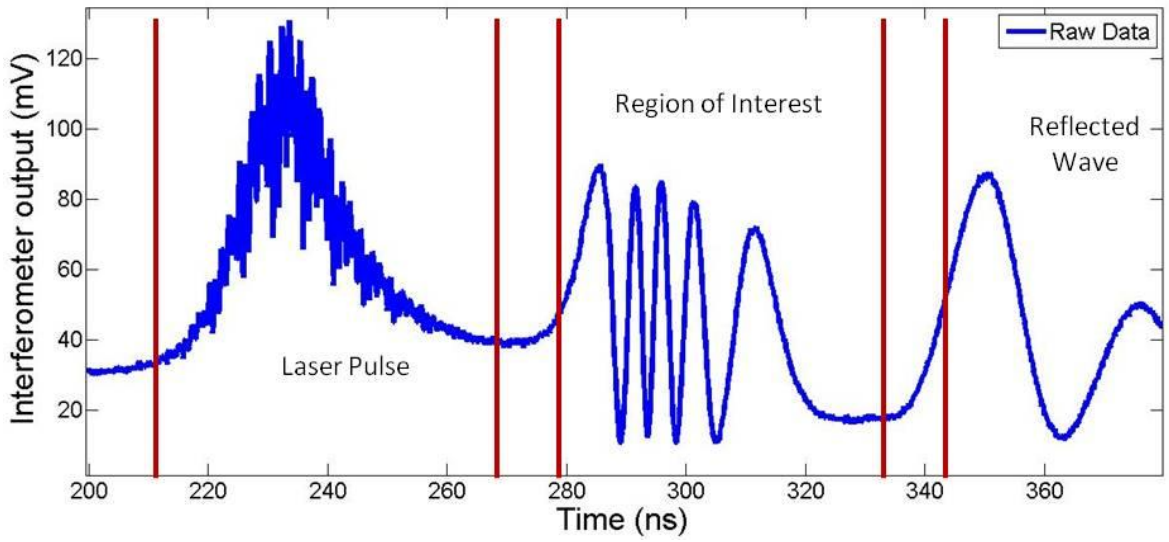

Figure 2.7: Typical recorded laser loading light intensity signal. The Nd:YAG laser pulse is sensed by the photodetector (shown as "Laser Pulse") prior to the arrival of the stress wave on the free surface (shown as the "Region of Interest"). After the region of interest the stress wave that has reflected within the material is recorded.

During a typical laser loading test the laser is triggered to fire at (arbitrarily set) time zero, but through electrical delay the laser Q-switch opens 200 ns later releasing the laser energy. Since silicon, the typical specimen substrate material of interest in this study, is transparent to IR radiation, the photodetector almost instantaneously records the profile of the laser pulse (shown as "Laser Pulse" in Figure 2.7), followed, after the time necessary for the much slower stress wave (8400 m/s) to travel across the silicon substrate thickness, by the out-of-plane displacement of the free surface of the specimen. The out-of-plane displacement can be seen in Figure 2.7 as the peaks and valleys of the signal corresponding to successive constructive and destructive interferences in the sinusoidal signal between 275 and 325 ns. This sinusoidal signal is caused by the light interference along path C of the Michelson interferometer. A local maximum indicates constructive light interference, and a local minimum indicates destructive light interference. The sinusoidal portion of the signal is the region of the greatest interest for obtaining the profile of

the stress wave caused by the laser loading method. The out-of-plane motion begins 60 ns after the firing of the laser, matching the time necessary for a wave to propagate through the thickness of a specimen. Once the free surface motion subsides, the recorded light intensity remains at a constant value until the initial stress wave has reflected within the sample, back to the free surface. At that point the light intensity becomes sinusoidal again with the free surface moving out-of-plane (see "Reflected Wave" in Figure 2.7). As the stress wave reflects through the sample dissipation takes place leading to diminishing levels of free surface motion.

2.3 Signal Analysis – Measurement Principles

The region of interest for the laser loading method from Figure 2.7, is shown in Figure 2.8.

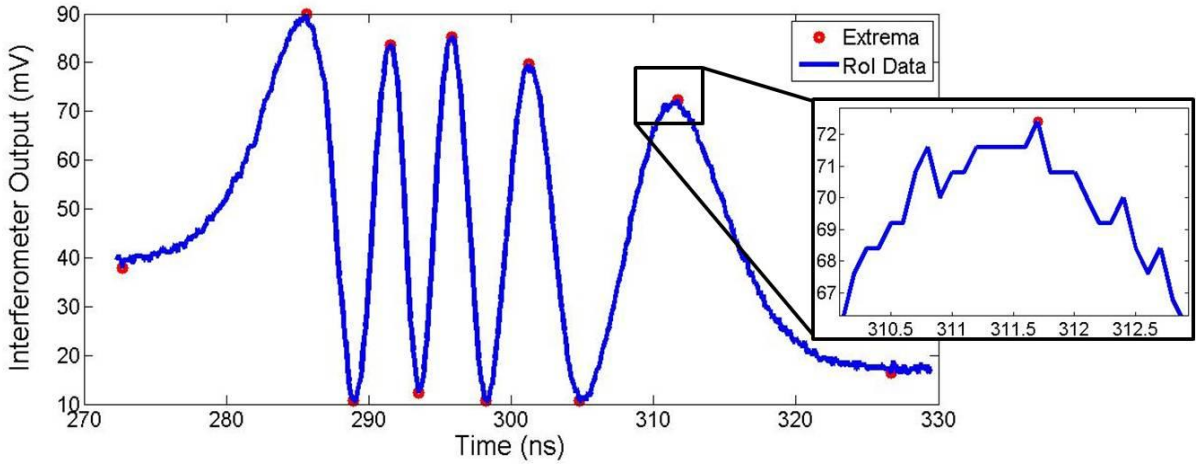

Figure 2.8: Michelson raw light interference data of the region of interest (out-of-plane motion of the specimen free surface), with zoomed in region of extrema. Extrema indicated by red circles do not fall at the center of a peaks and troughs because of inherent noise in the recorded signal.

The sinusoidal signal is converted to an interference fringe count through

$$I(t) = \frac{I_{max} + I_{min}}{2} + \frac{I_{max} - I_{min}}{2} \sin(2\pi f(t) + \phi) \,, \qquad (2.2)$$

where I_{max} and I_{min} are the maximum and minimum intensity of the fringes measured by the photodetector, $f(t)$ is the fringe count at time t, and ϕ is the phase angle of the signal (Yuan and Gupta, 1993). The interference fringe count allows for the displacement of the free surface to be found at each recorded point in time when applied to Equation 2.3 below:

$$u_{fs}(t) = \frac{\lambda}{2} f(t) \,, \qquad (2.3)$$

One complete fringe corresponds to a displacement of 266 nm, half the Michelson laser wavelength. Figure 2.9 displays the interference fringe count and displacement corresponding to the raw data signal shown in Figure 2.8.

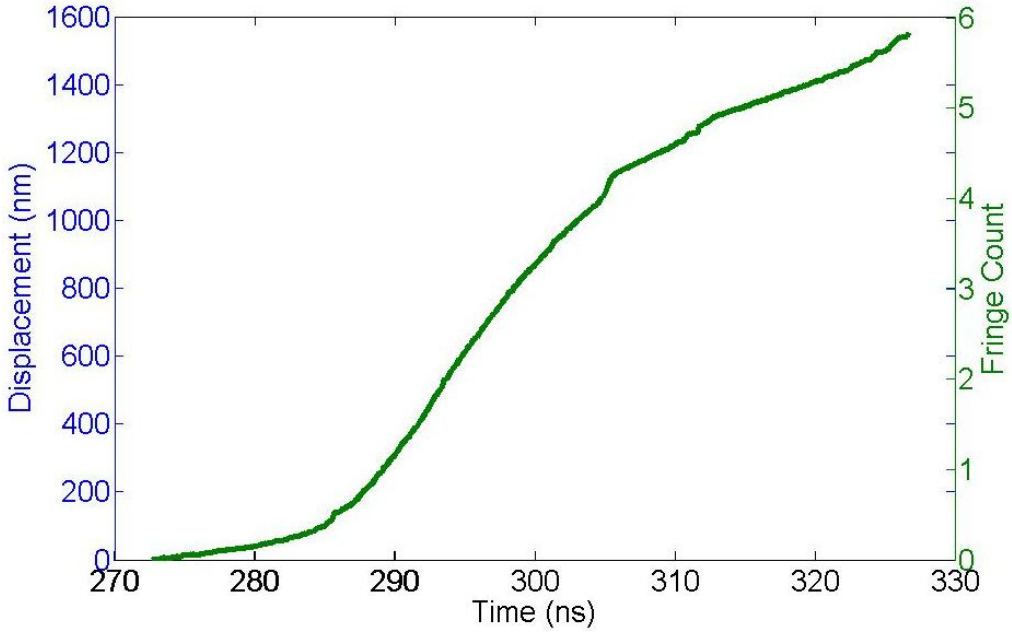

Figure 2.9: Interference fringe count and displacement data of the out-of-plane motion of the specimen free surface.

A smoothing spline curve fit is applied to the displacement data, and then differentiated with respect to time to obtain the free surface velocity. The smoothing spline curve fit and differentiation are executed using a MATLAB software package. The stress history is obtained from the velocity data through Equation (2.1). Figure 2.10 shows the velocity and stress profile corresponding to the raw data signal shown in Figure 2.8.

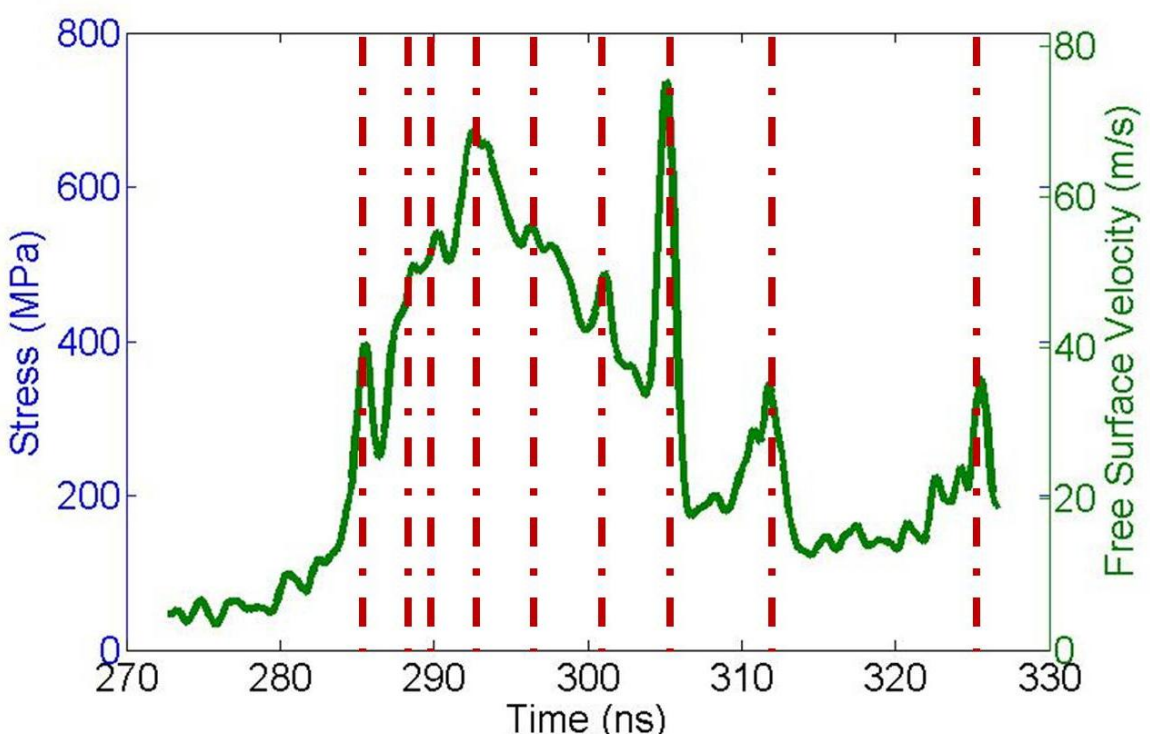

Figure 2.10: Velocity of the specimen free surface and the determined stress from laser loading. Red dashed lines indicate the time at which extrema were found in the raw Michelson Interferometer data.

Although the stress profile should follow a similar contour of the energy released by the Nd: YAG laser, as seen in Figure 2.7, on many occasions the profile may display additional peaks, such as at 305 seconds where the free surface comes to a nearly velocity free state then dramatically increases to a peak velocity of 723 MPa over 1.5 ns. Such discrepancies form the expected profile, which are outcomes of the discrete data differentiation, highlight the need to

improve the data analysis approach previously used by Yuan and Gupta (1993), Wang (2002) and Kimberley (2008). The dashed vertical lines placed on Figure 2.10 correspond to the position of the extrema show in Figure 2.7. Around each of the extrema the stress profile demonstrates the odd peaks previously mentioned, demonstrating the effects of noise when differentiating the displacement signal to obtain the stress and velocity profiles.

Here an investigation was conducted to find a data analysis approach that would reduce the effects of noise in the recorded Michelson interferometer raw data signal that translates to spikes in the stress and velocity profiles. The improved data analysis method used to analyze the recorded signal relies on using a moving average filter to reduce the effects of inherent signal noise without compromising the integrity of the recorded signal. The moving average filter is only applied over a selective region around the extrema points (see Figure 2.8) in the raw data signal; the data points between the extrema do not significantly contribute to the unwanted behavior in the stress profile, as seen in Figure 2.10. The moving average filter is applied over a region of 15, 30 or 45 points, with the extrema fixed as the midpoint of the averaging region. The averaging region chosen must the largest averaging region that is less than the lowest number of data points between extrema. Within the averaging region the number of point used in the moving average filter is chosen as one third of the averaging region length.

The result of the moving average filter on the raw data signal originally shown in Figure 2.8, is shown in Figure 2.11, where both the non-averaged and averaged signals are overlaid. A zoomed in view of the extrema located at 305 ns is shown in Figure 2.11(b) to highlight the effects of the filtering. The extrema within the region changes slightly, and the resulting signal in the averaging region more closely follows the contour of a sinusoidal signal near the extrema.

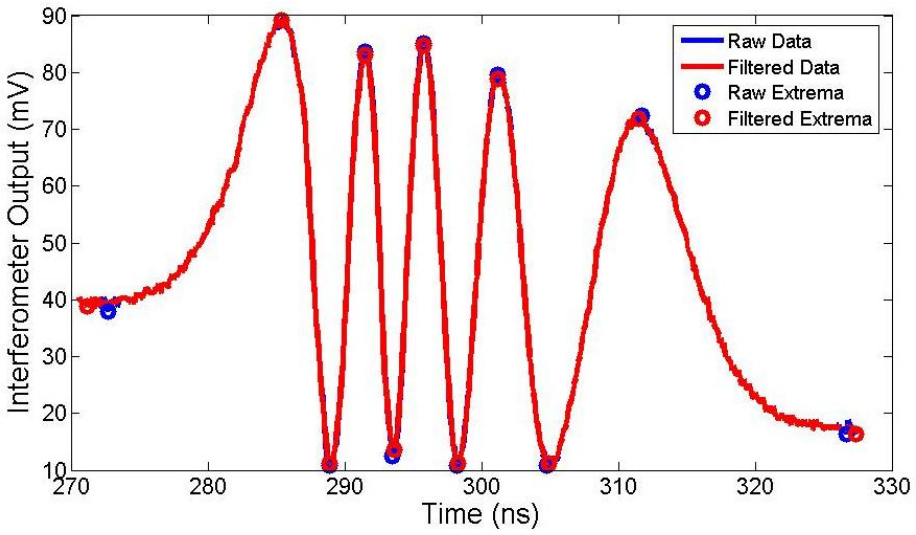

(a)

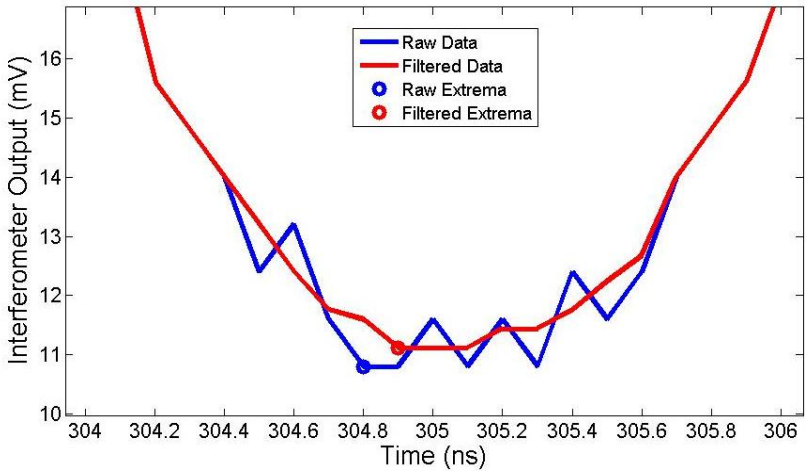

(b)

Figure 2.11: A comparison of the raw Michelson interferometer data and the moving average filtered Michelson data (a) The Michelson raw light interference (blue) and the moving average filtered light interference (red) data of the region of interest, showing that the filtered data closely matches the raw signal (b) A zoomed in view around the extrema located at 305 ns, displaying the reduction of noise, and the sinusoidal shape of the filtered data around the extrema.

The resulting displacement from the averaged raw data signal is compared to the displacement found without averaging in Figure 2.12. The displacement jumps that occur in the

non-averaged signal are significantly reduced and in some places entirely removed, such as at 286 ns, 305ns, and 312 ns.

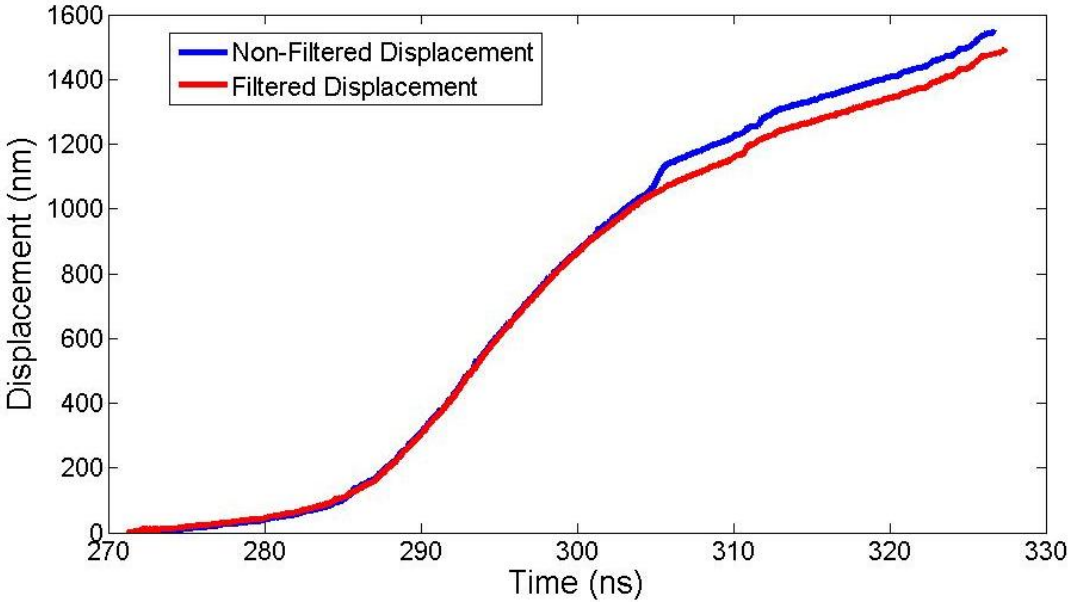

Figure 2.12: A comparison of the non-averaged (blue) and the moving average filtered displacement data (red). The moving average filtered demonstrates the ability of the improved analysis method to remove undesirable features.

The displacement shown in Figure 2.12 is then differentiated in MATLAB using a smoothing spline fit to the displacement data obtained after applying the moving average filter around to the raw data, to determine the stress profile. The stress profile of the raw data and the extrema smoothed data are presented in Figure 2.13. The spikes in the stress profile are significantly reduced producing a stress profile that more closely matches the laser pulse profile.

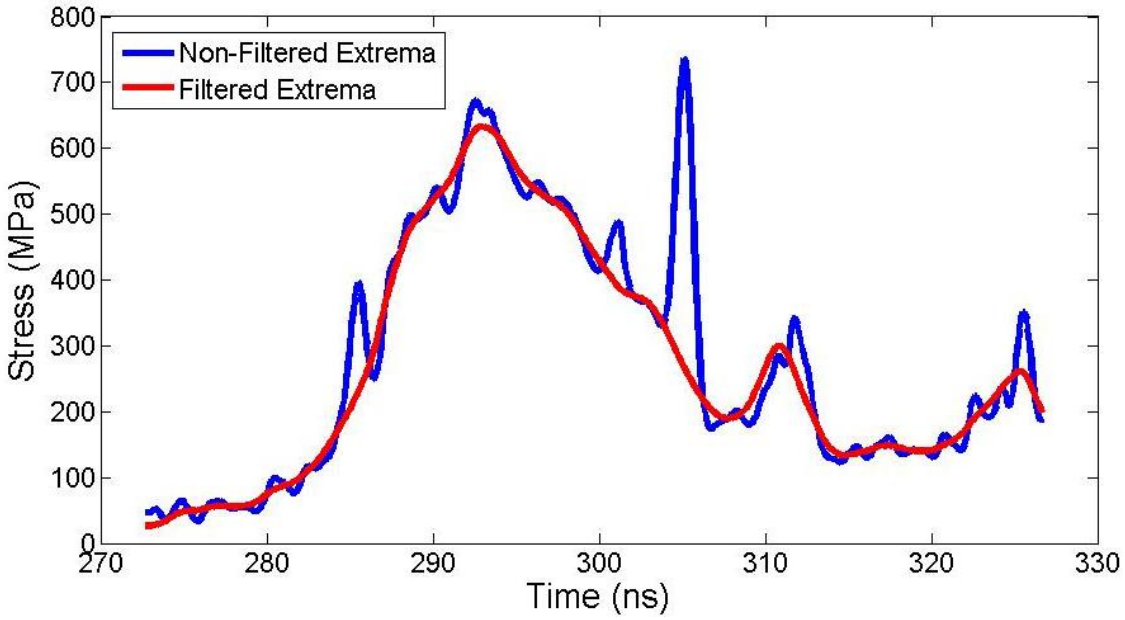

Figure 2.13: A comparison of the velocity and stress profiles obtained from moving average filtered displacement data and raw displacement data. The moving average data removes the spiking in the stress profile, primarily those at 286 ns and 305 ns.

The ability of the improved method to remove the effects of noise on the stress measurement is of particular importance to the work conducted here because the results of experiments will be compared to simulations that require an accurate input of the stress wave magnitude and profile applied to the specimen.

Chapter 3: Calibration Specimen Fabrication

To obtain the profile of stress waves produced at varying levels of laser fluence, calibration specimens are required with well controlled specimen characteristics, that when tested will provide repeatable results with minimal variations. Figure 3.1 shows a side view of the typical 12 mm x 12 mm specimen layup for the stress wave calibration specimens.

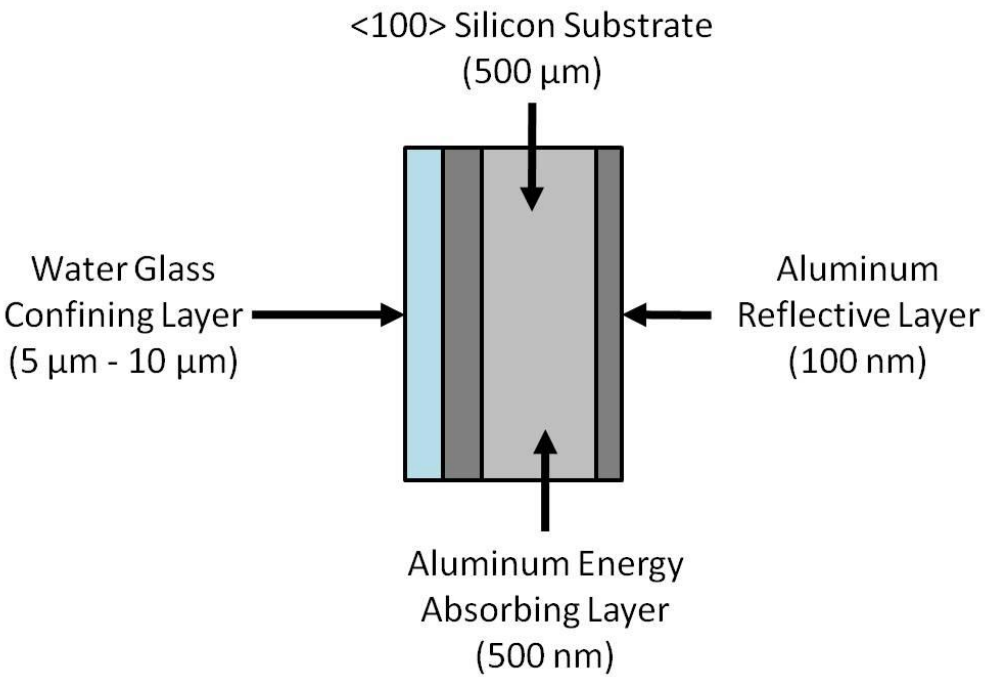

Figure 3.1: Calibration Specimen Layup

3.1. Energy Absorbing and Reflective Layer Deposition

Specimens were prepared for laser loading by first depositing the aluminum laser energy absorbing layer on a substrate, typically a four inch <100> silicon wafer 500 µm in thickness and of prime grade. The aluminum energy absorbing layer was deposited to a thickness of 500 nm. Previous work by Yuan *et al.* (1993) points to an aluminum energy absorbing layer of 500 nm because it creates a consistent and repeatable stress wave profile when ablated during laser

loading. The energy absorbing layer of aluminum was deposited with an electron beam deposition system (Temscal 4-pocket) at the Fredrick Seitz Materials Research Laboratory Microfabrication facilities. The electron beam deposition process was chosen because it allows for relatively thick metallic layers, on the order of 1 μm, to be deposited quickly. A deposition rate of 2 Å/s, measured using a quartz crystal monitor, was used for all aluminum depositions. The aluminum source target was warmed for at least 15 minutes prior to each deposition to ensure an even deposition rate. After each metallic deposition, the deposited layer thickness was measured using a Dektak 3030 profilometer. A profilometer drags a 5 μm diameter tip stylus across a surface, providing a resolution of tens of nanometers of the surface profile. Deposition thicknesses vary because of changes in the electron beam profile after equipment servicing, thus deposited layer thicknesses measured by the crystal monitor need to be verified accordingly. In Figure 3.2, recorded profilometer scans versus length in the vicinity near an edge of the deposited Al layer, showing an aluminum deposition thickness of 500 nm, are illustrated.

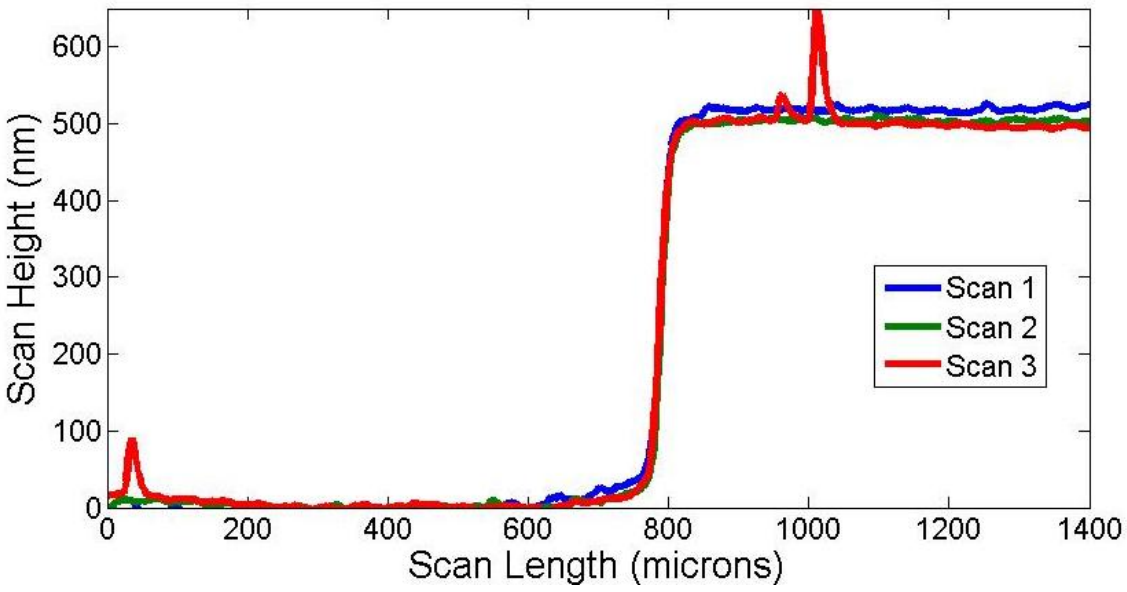

Figure 3.2: Profilometer scan of Aluminum deposition thickness.

Deposited metal thicknesses are treated as uniform for the work presented here, when in actuality they show variation over the deposited surface. Figure 3.2 shows the profilometer scan along three parallel lines on the deposited surface. For each deposited wafer sample three such scans were performed, and the deposition thickness was calculated as the average measured layer thickness, for example the region between 800 and 1400 microns in Figure 3.2 would be averaged to a measured thickness of 500 nm. Due to the variability of electron beam deposition calibration specimens had average deposited energy absorbing layer thicknesses between 450 and 550 nm.

After depositing the energy absorbing layer, a reflective layer of 100 nm of aluminum is deposited on the back side of the sample (Figure 3.1). This reflective layer increases the amplitude of the recorded Michelson interferometer signal by a factor of two, compared to the interferometer signal reflected from bare silicon. A reflective layer thickness of 100 nm was

chosen because testing showed that a layer of this thickness would not spall under laser loading conditions.

3.2 Confining Layer Application

After the metallic depositions, the silicon wafer substrate is placed into an SCS 6800 spin coater and the energy absorbing layer is covered with 10 ml of waterglass using a digital pipette. Waterglass is a viscous sodium silicate solution that dries to form sodium silicate glass. The silicon wafer is rotated by the spin coater to a high speed (1,000 to 4,000 rpm) in a process known as spin coating, causing the waterglass to spread over the surface to a nominally uniform thickness (Madou, 2002). In the spin coating protocol employed here the substrate is covered with a viscous liquid, then accelerated for 10 seconds to a dwell speed that is held for 120 seconds allowing the liquid to spread over the substrate to a uniform thickness. In general, higher dwell speeds lead to thinner coating thicknesses. After spin coating the waterglass is left to dry for an additional 2 hours, completing the confining layer application process.

It is clear that the thickness of waterglass will directly affect the magnitude of the compressive stress wave generated in the substrate during laser loading since a thicker confining layer will constrain the energy absorbing layer ablation more, thus causing a more intense stress wave to be generated in the substrate. Thus if we are to achieve a repeatable stress wave travelling in the silicon substrate for a given laser intensity, the waterglass confining layer thickness must be well characterized. A parametric study was conducted to determine the thickness and the repeatability of waterglass coatings created via the spin coating process. In total, 30 silicon substrates measuring 20 mm by 20mm were coated with an energy absorbing layer nominally 500 nm thick. The substrates were then split into six groups of five samples

each, and each group was spin coated with dwell speeds of 1000 rpm, 1250 rpm, 1500 rpm, 2000 rpm, 3000rpm, and 4000 rpm. After drying, each of the spin coated samples was scanned using a Dektak 3030 profilometer to obtain the thickness and repeatability of the spin coated waterglass layers. A typical scan of waterglass thickness is shown in Figure 3.3.

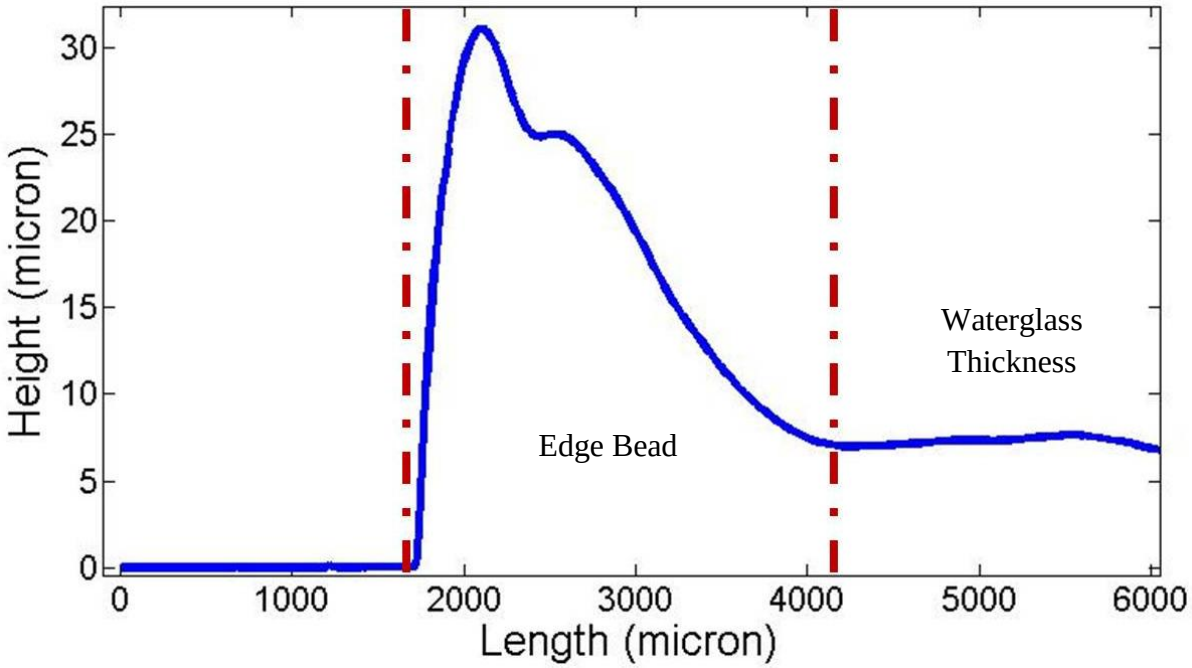

Figure 3.3: A profilometer scan of spin coated waterglass. The region located between the two dashed red lines is the edge bead of the waterglass. The waterglass that is present over calibration samples is indicated in the "Waterglass Thickness" region of the profilometer scan. The waterglass thickness is assumed to be nominally consistent over the regions unaffected by the edge bead .

During spin coating, as the waterglass spreads over the surface an edge bead is formed, the region between the dashed red lines in Figure 3.3 labeled "Edge Bead". The edge bead thickness is much greater than the thickness of the waterglass away from the edge bead. To overcome edge bead effects entire silicon wafers are spin coated at one time, and specimens at the edges of the silicon wafers are discarded. The region of Figure 3.3 labeled "Waterglass Thickness" is the thickness of the waterglass that creates the confining layer. Figure 3.4 shows

the measured waterglass thicknesses, as indicated by the circle data points, as a function of spin coating speed. The average thicknesses for each spin coating speed are connected with a black line.

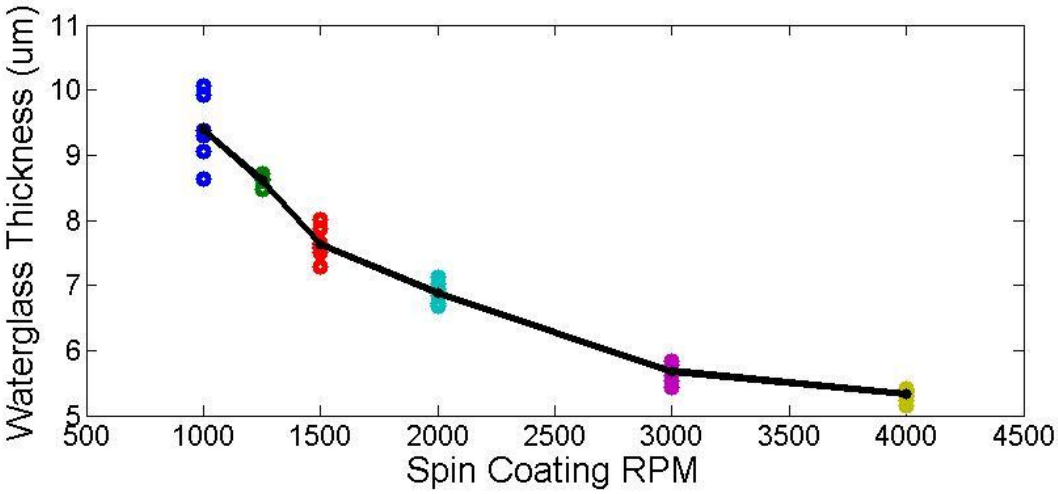

Figure 3.4: Waterglass thickness. Each circle indicates a measured thickness from a profilometer scan. Average values for each of the spin coating speeds are connected by black lines.

The limited spread in the measured waterglass thicknesses at spin coating speeds greater than 1000 rpm shows the highly repeatable nature of the spin coating process, making it a highly attractive method to adequately control waterglass application. Analysis of the measured spin coating thicknesses obtained can be seen in Table 3.1.

Table 3.1: Measured Waterglass Thickness Data

Waterglass Spin Coating Speed (rpm)	Average Waterglass Thickness (µm)	Thickness Standard Deviation
1000	9.39	0.53
1500	8.61	0.21
2000	7.62	0.13

At a spin coating speed of 1000 rpm the centripetal force created is not great enough to overcome the viscosity of the waterglass, preventing even spreading of the waterglass over the substrate surface, which is verified by this spin coating speed producing waterglass thickness with the greatest standard deviation.

3.3 Sample Cleaving and Cleaning

After waterglass application, the silicon wafer is cleaved using a diamond tip scribe into 12 mm by 12mm samples, a typical four inch wafer yields 48 samples. After cleaving, the reflective layer of each calibration specimen is cleaned using acetone, isopropyl alcohol, and cotton swabs. Cleaning the reflective layer increases the amplitude and reduces the measured noise in the recorded interferometer signal.

3.4 Waterglass Thickness Investigation

Calibration specimens were manufactured with waterglass thicknesses resulting from 1000, 1500, 2000, and 2500 rpm. These four waterglass thicknesses were chosen because previous work conducted by Kimberley (2008) produced successful laser loading experiments using water glass thicknesses achieved with these spin coating speeds. The specimens were subjected to levels of laser energy between 30% and 100% in increments of 10%, to determine the level of laser energy that a specimen can sustain before cleaving or spallation occurs.

The selected values used for testing are shown in Figure 3.5 as yellow boxes.

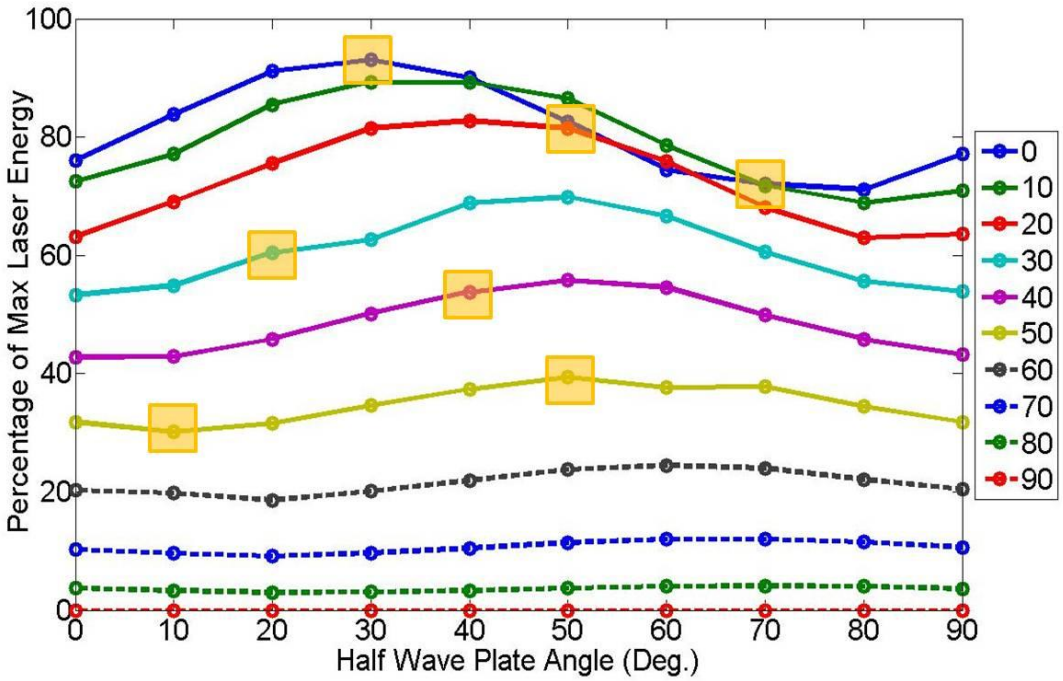

Figure 3.5: Waterglass investigation energy levels. Spin coated waterglass samples were tested at energy levels indicated by yellow squares.

The results of the number of surviving specimens, i.e., those not showing cleaving or spallation, as a function of varying laser energy are summarized in Table 3.2

Table 3.2: Surviving Waterglass Specimens (out of a total of 5 tested at each setting)

Laser Energy Level (%)	Waterglass Spin Coating Speed			
	1000 rpm	1500 rpm	2000 rpm	2500 rpm
100	0	0	0	0
90	0	0	0	0
80	0	0	0	0
70	0	0	1	1
60	0	1	2	4
50	0	2	3	5
40	3	5	5	5
30	4	5	4	5

For the 1000 rpm samples (9.39 µm waterglass thickness) failure started occurring at energy levels above 40%. For the 1500 rpm samples (8.61 µm waterglass thickness) failure started

occurring above 50% laser energy, for 2000 rpm and 2500 rpm failure began occurring above70% laser energy. From the waterglass thickness investigation a spin coating speed of 2000 rpm was selected for use on all calibration specimens. It was selected because it showed the lowest standard deviation over the measured waterglass thicknesses, as shown in Table 3.1, and could be subjected to a satisfactory rage of laser energy before sample failure.

After selecting the waterglass thickness (7.62 μm) obtained from spin coating at 2000 rpm, calibration specimens were made for testing in order to obtain the temporal profile of the stress waves created via laser loading at various levels of fluence. The results of those experiments are described in the next chapter.

Chapter 4: Calibration Specimen Testing Results

The initial waterglass thickness investigation, as described in section 3.4 provided an upper bound on the level of laser energy that a specimen could sustain before spallation. Calibration specimens were subjected to levels of laser energy between 30.1% and 55.8%, in increasing increments of a few percent to obtain the temporal stress wave profile at each laser energy level. The selected energy values used in this series of experiments are shown graphically in Figure 4.1 as blue squares, and are listed in Table 4.1.

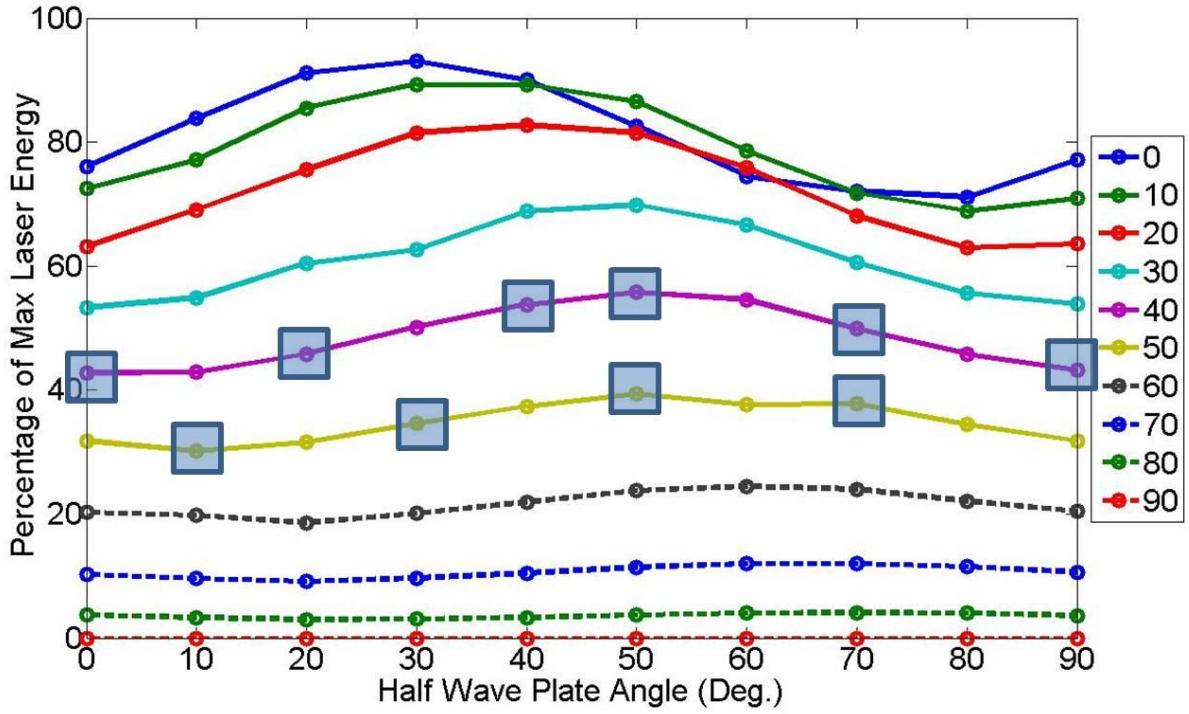

Figure 4.1: Laser energy values selected for test calibration specimens

Table 4.1: Laser Energy Percentages Tested

Polarizer Angle (Deg.)	Wave Plate Angle (Deg.)	Percentage of Laser Energy Maximum
40	50	55.8
40	40	53.8
40	70	49.9
40	20	45.8
40	0	42.8
50	50	39.4
50	70	37.8
50	30	34.6
50	90	31.8
50	10	30.1

Approximately ten calibration samples were subjected to each of the laser energy levels indicated in Table 4.1. The interferometer data collected for each of these tests was analyzed using the improved data analysis approach as explained in section 2.3, to obtain the stress wave profile created at each laser energy level.

4.1 Stress Wave Profiles

Testing conducted at laser energy levels of 53.8 and 55.8 % resulted in all of the tested samples showing signs of cleaving and spallation or both. Samples that show spallation or cleaving are not used for data analysis. Calibration samples tested at energy levels below 53.8% did not show signs of spallation. At each energy level the recorded interferometer signals of each test were analyzed individually using the method outlined in section 2.3 to obtain the temporal profile of the stress wave. The stress wave arrival times show slight deviations, between 2 and 4 nanoseconds at most, most likely because of the electrical delay of the Q-Switch opening within the Nd:YAG laser. For plotting the results together, as seen for example in Figure

4.2 for one particular energy level, each curve is shifted in time so that the peak values of each stress wave profile occur at the same time. In this fashion we can examine the repeatability of the rise and the decay times of the stress profile of nominally identical experiments. The time shifted stress wave profiles for the tests conducted at 49.9% of the laser energy are shown in Figure 4.2.

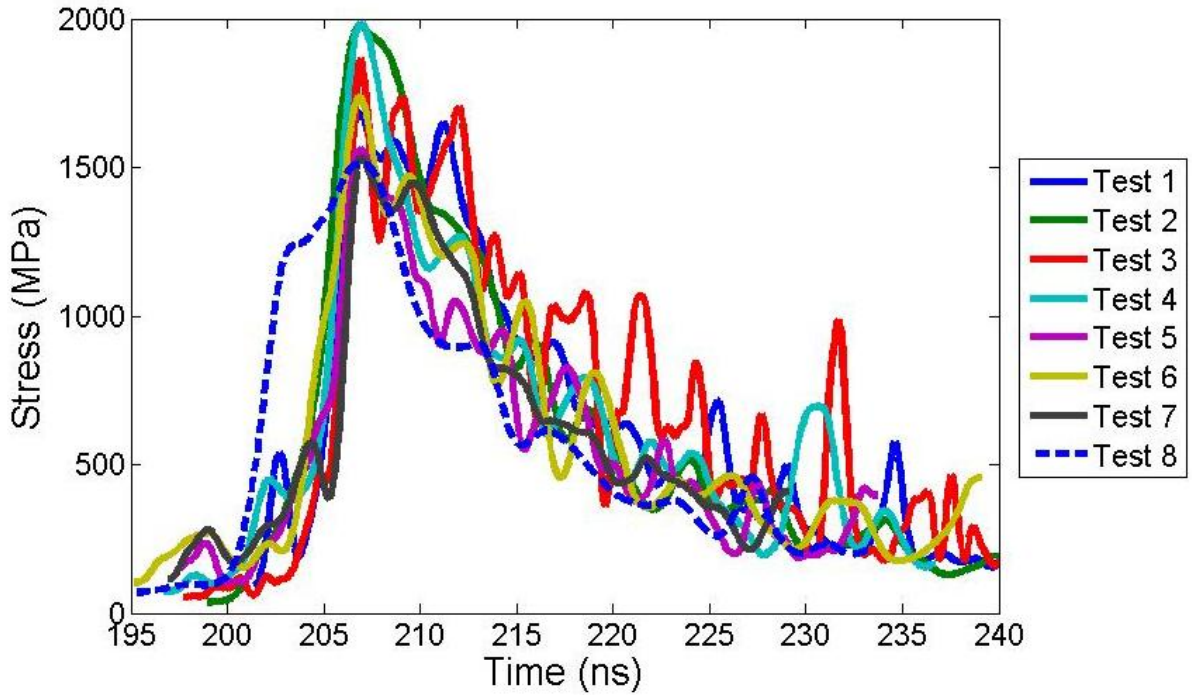

Figure 4.2: Stress profiles acquired from samples subjected to 49.9 % laser energy

It can be seen from Figure 4.2 that although the rise and decay times are comparable among different runs of a nominally identical sample, there is a spread in the peak stress value among these cases – a minimum of 1511 MPa and a maximum of 1985 MPa being recorded for this laser power level. The reason for this spread is because of the variability of the metallic depositions (refer to Figure 3.2), water glass thickness (refer to Figure 3.4) and the level of laser energy released by the Nd:YAG laser in each pulse which can vary by $\pm$ 1 % according to manufacturer specifications.

The processes developed in chapter 3 are used to limit the variations between samples as much as possible. Despite the variation of the maximum amplitude of the stress profile, the stress profiles do show similar characteristics such as the rise time to the maximum stress (~8 ns), and decay time (~20 ns). The following figures (4.3 through 4.9) show the stress profiles obtained from the laser energy levels below 49.9%. Note that each of the laser energy levels continue to show a similar rise and decay profile to the 49.9% energy level testing.

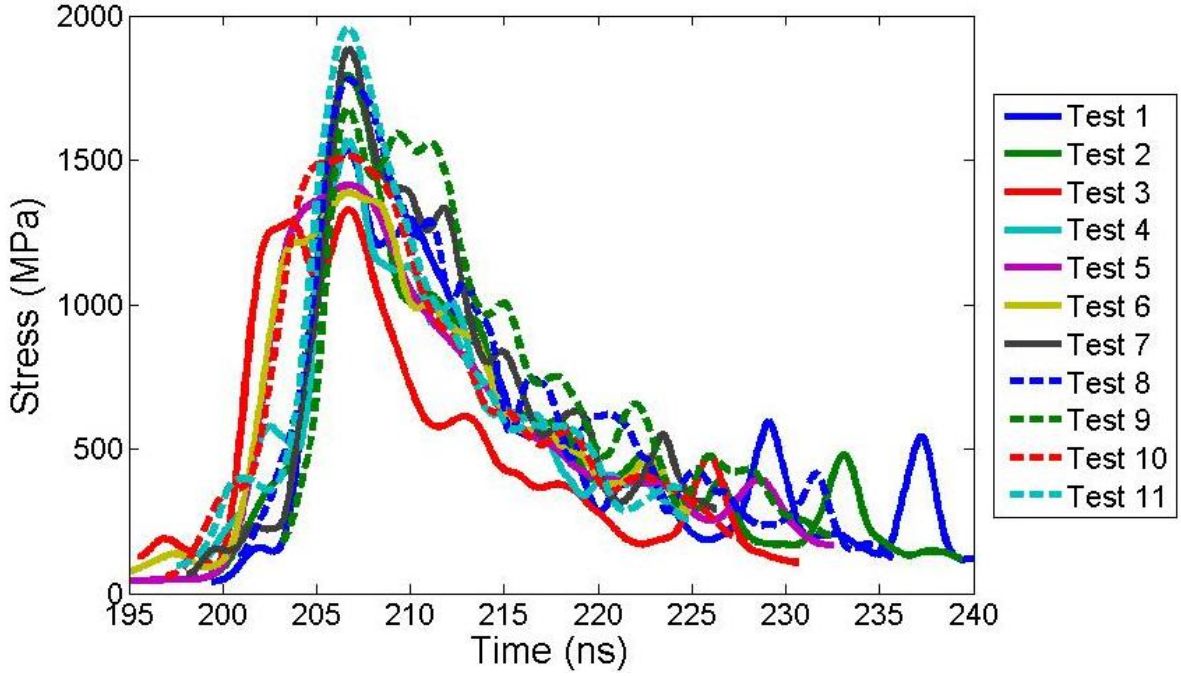

Figure 4.3: Stress profiles acquired from samples subjected to 45.8 % laser energy

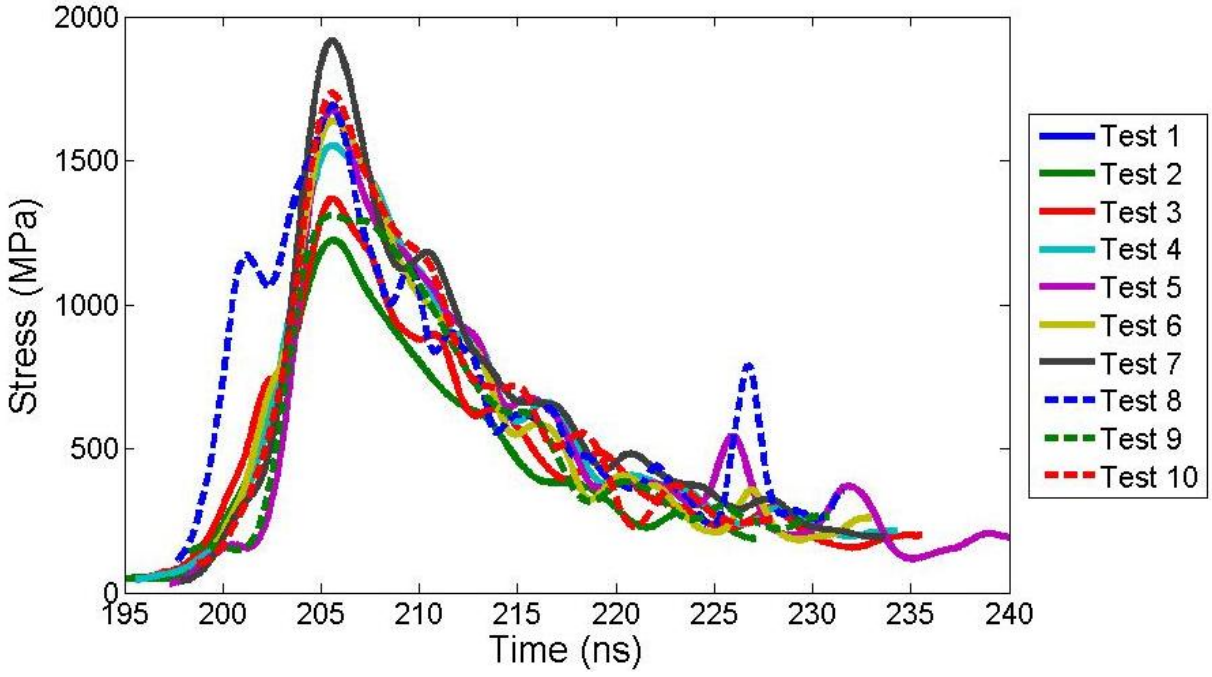

Figure 4.4: Stress profiles acquired from samples subjected to 42.8 % laser energy

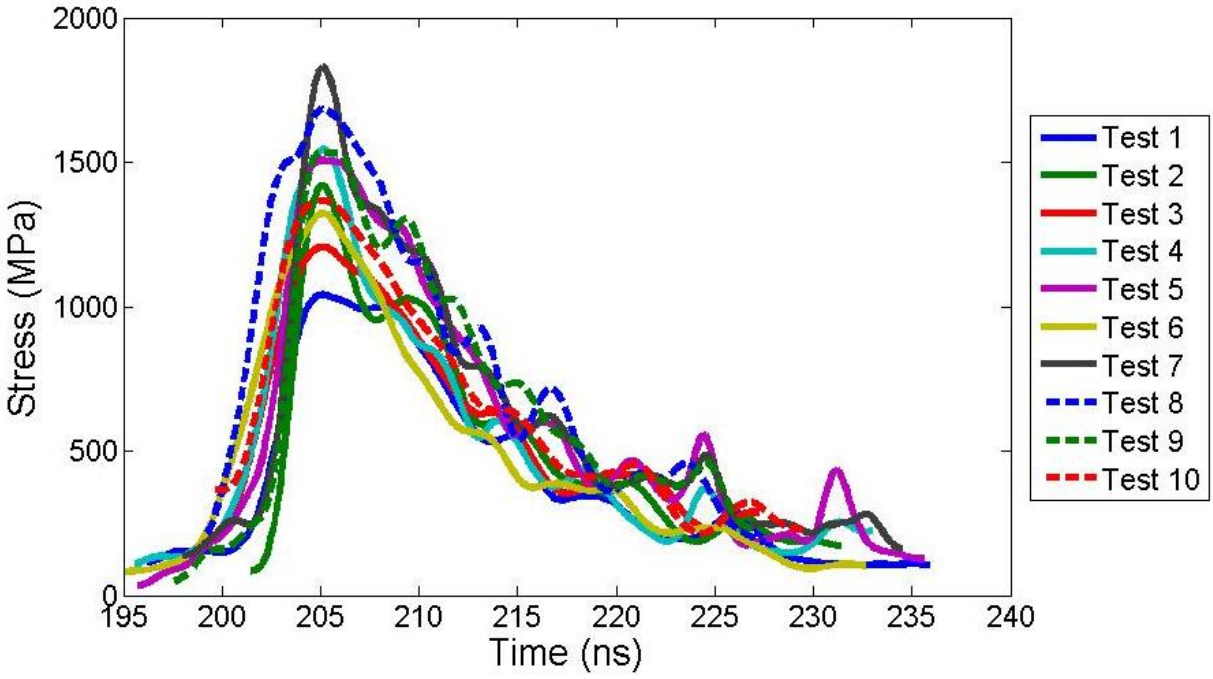

Figure 4.5: Stress profiles acquired from samples subjected to 39.4 % laser energy

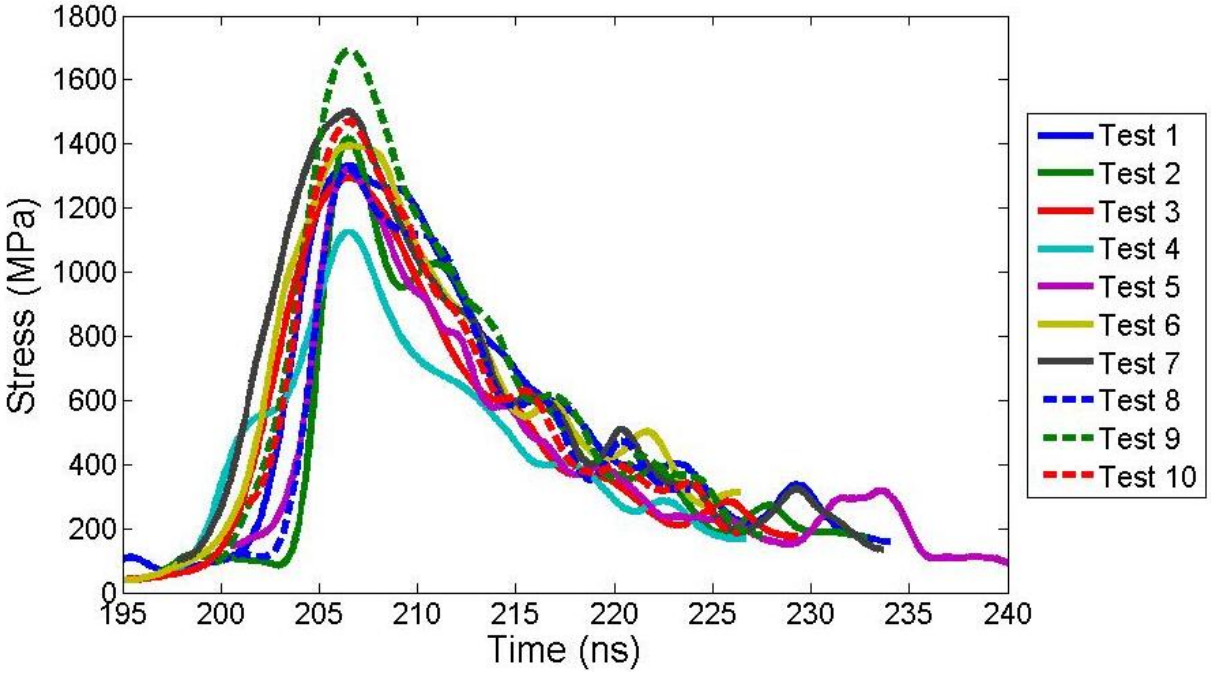

Figure 4.6: Stress profiles acquired from samples subjected to 37.8 % laser energy

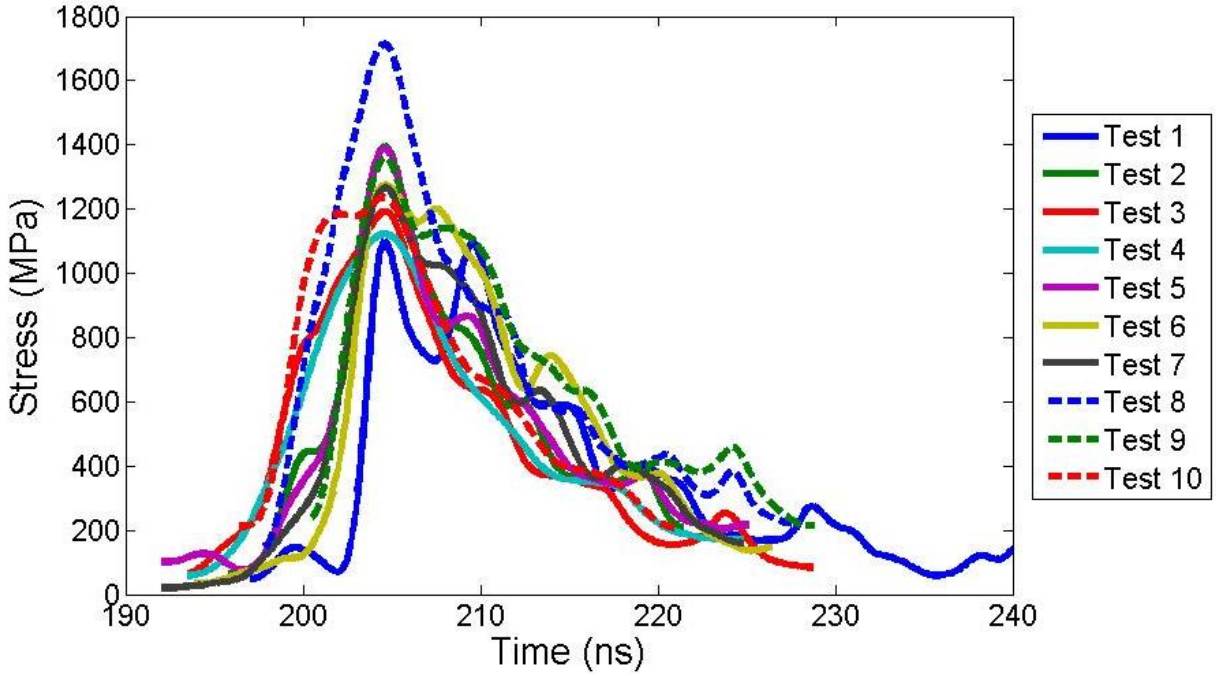

Figure 4.7: Stress profiles acquired from samples subjected to 34.6 % laser energy

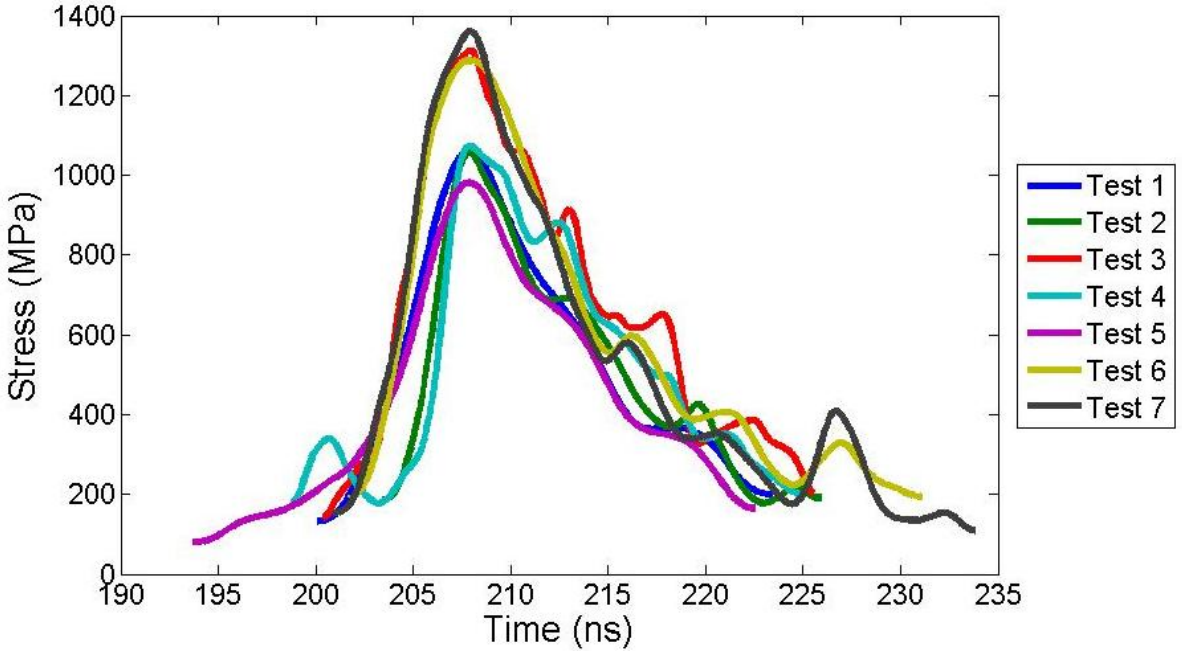

Figure 4.8: Stress profiles acquired from samples subjected to 31.8 % laser energy

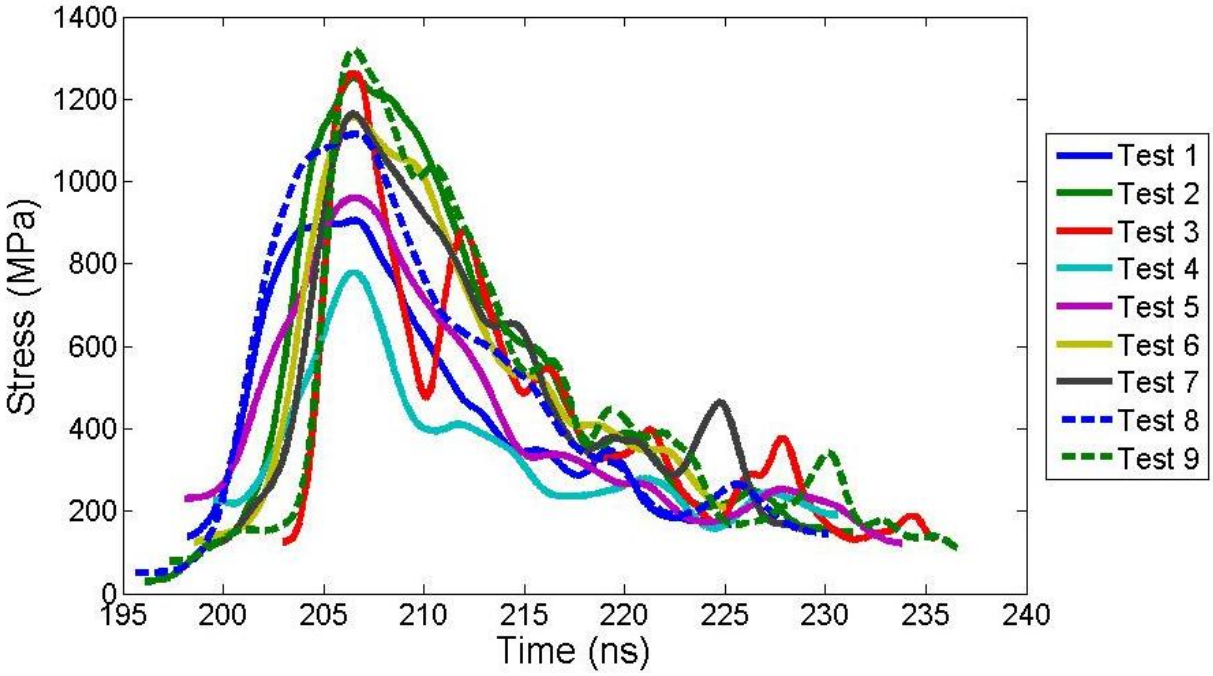

Figure 4.9: Stress profiles acquired from samples subjected to 30.1 % laser energy

From this sequence of results it is clear that the peak stress decreases with decreasing laser power, although there is a spread in peak stress values. Figure 4.10 shows the increasing peak stress dependence on increasing laser power. The spread of the maximum stress values is shown for each laser energy as scatter bars. The average values are connected through the line shown in the figure. The stress profile spread at each of the laser energy levels is relatively consistent. The average values of the maximum stress do show a nearly linear increase between 30.1% and 49.9% power.

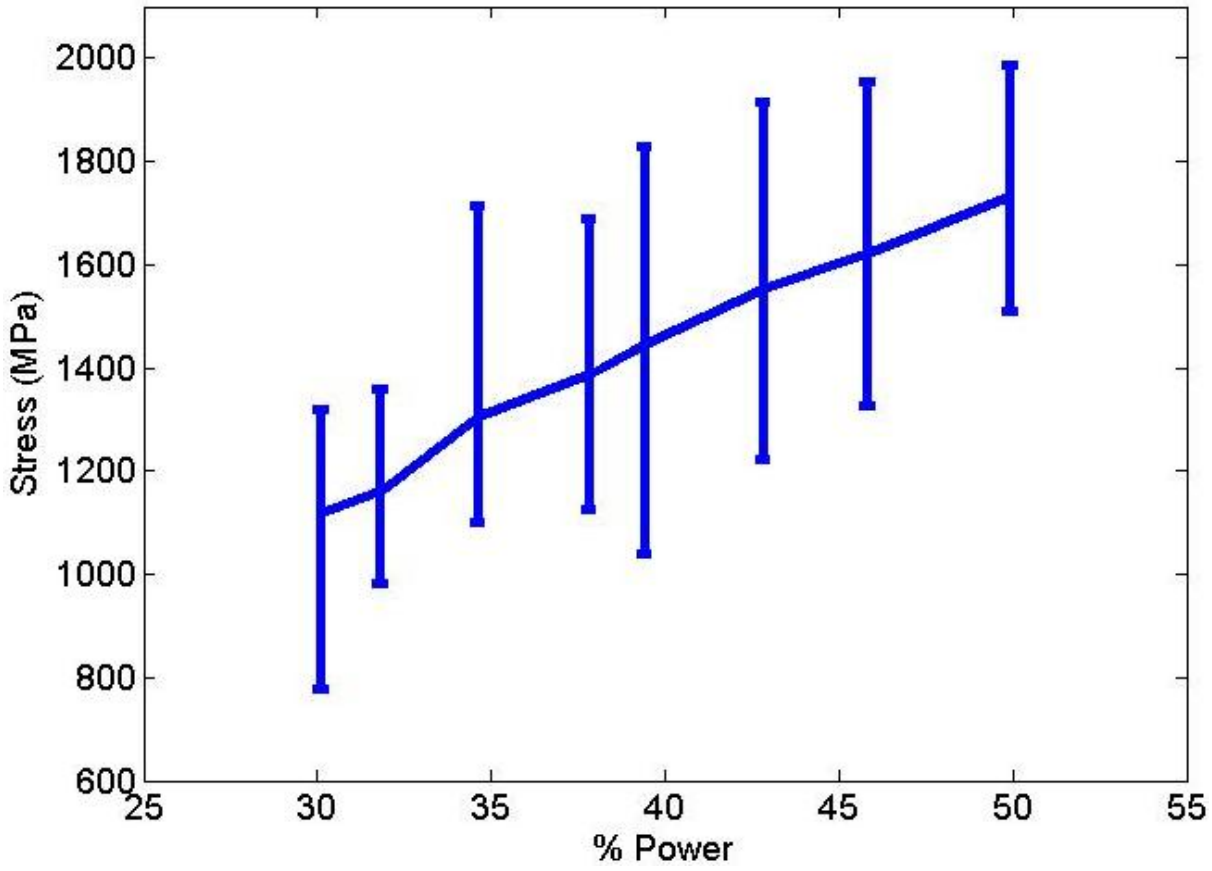

Figure 4.10: Spread of maximum stress values of calibration specimen, connected by average maximum stress values

For the numerical simulations of interest a precise temporal stress variation is required as input. Thus, an *average* profile of the stress waves for each laser energy level was obtained by

averaging the individual stress profiles shown in figure 4.3 through figure 4.9. The average stress profiles are presented together in Figure 4.11, with the stress profiles shifted for clarity purposes by an (arbitrary) amount relative to the laser energy level.

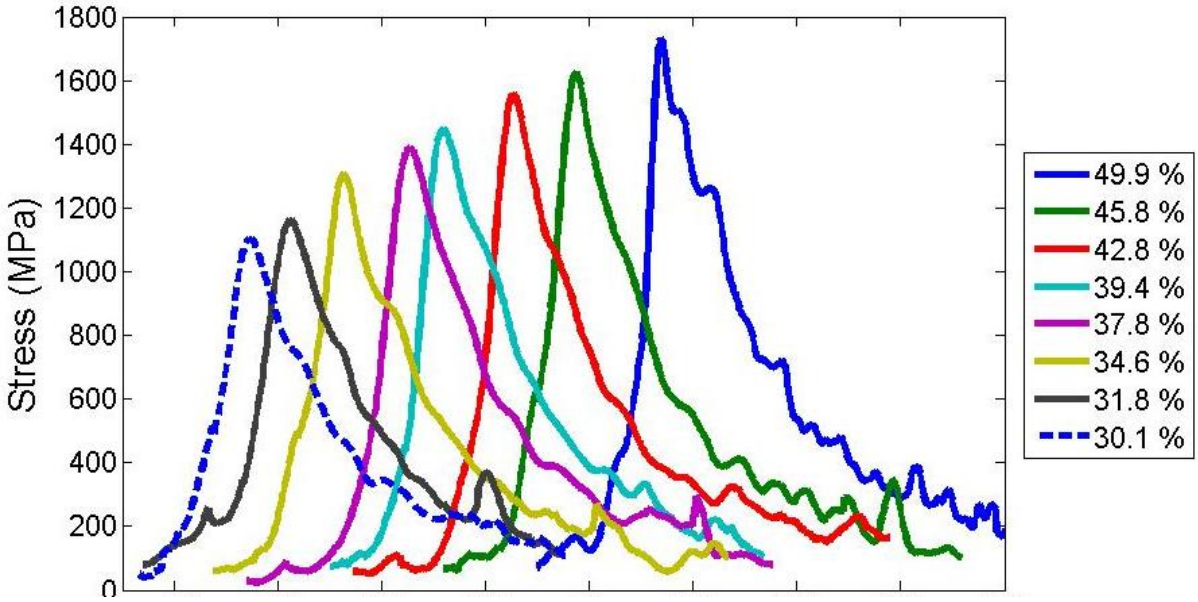

Figure 4.11: Average stress profiles for laser energy levels between 30.1% and 49.9%

The average stress profiles show similar rise times and similar decay profiles. The rise time of each of the average stress profiles was determined by calculating the time from the initial minimum stress value to the maximum stress value. The stress wave decay time was calculated as the amount of time between the maximum stress value and twenty percent of the maximum stress value. A summary of the rise time and decay time measurements can be found in Table 4.2.

Table 4.2: Average Stress Wave Characteristics

Laser Energy % Tested	Stress Wave Rise Time (ns)	Stress Wave Decay Time (ns)
49.9	8.0	19.6
45.8	8.6	17.6
42.8	8.3	18.0
39.4	8.4	18.1
37.8	8.7	17.9
34.6	8.8	17.2
31.8	7.5	16.0
30.1	8.5	18.0

It is important to note the similarity in the stress wave rise times and decay times between the different levels of laser energy. From the determination of the rise times and the decay it can be seen that even though there is variability between specimens of the deposited metallic layer thickness and waterglass thickness, the general loading shape of the stress wave is maintained.

From this study it has been shown that with careful control of the sample fabrication methods used as well as careful control of the loading process that repeatable stress wave profiles can be achieved. The repeatability of the stress waves in this study provides great promise for the use of laser loading in future applications that do not allow for the out-of-plane displacement of the free surface to be measured. Such applications will be explained in section 5.2.

Chapter 5: Conclusions and Future Work

5.1 Concluding Remarks

The main goal of the work presented in this thesis was to evolve the high-power pulsed laser loading technique to have a highly repeatable temporal stress wave profiles created at different levels of laser energy over an almost continuous spectrum of power. This study is important because of the desire to fully understand the stress wave loading profile so experimental results can be *quantitatively* compared to computational models for sample geometries other than the simple one dimensional blanket films.

Through careful specimen design and fabrication, calibration specimens were developed that could be reproduced with minimal variation between them. Each of the required metallic depositions was characterized leading to the selection of an aluminum energy absorbing layer of 500 nm and a 100 nm aluminum reflecting layer. The waterglass confining layer thickness, 7.62 μm, created from a spin coating speed 2000rpm was chosen because it was high enough to overcome the viscosity effects of the waterglass and to be thick enough to allow testing to occur over a wide range of laser energies, 30% to 50%, without sample failure.

Testing of the calibration samples was conducted over a nearly continuous energy spectrum between 30% and 50% of the maximum laser energy. At each laser energy level approximately ten samples were tested, showing an average maximum stress value spread of 585 MPa. At 50% laser energy the average stress wave profile had a maximum value of 1731MPa, At 30% laser energy the average stress wave profile had a maximum value of 1101 MPa. Between 30% and 50% power, a linear relationship was found closely matching the maximum stress profile values, providing a relation of the laser energy and the average maximum stress profile

value. The average stress wave profiles for each laser energy level showed consistent rise times of 8 ns and decay times of 20 ns.

The results presented here are of importance because they can be applied to future studies of specimens manufactured on silicon substrates, such as blanket films and MEMS devices. Additionally the results are of importance because the stress wave that propagates through a laser loaded specimen no longer needs to be characterized for each individual test run, removing the need of the Michelson interferometer shown in Figure 2.2. With the removal of the Michelson interferometer form the test set-up it is possible to use other measurement techniques such as high speed imaging and digital image correlation to probe the displacement of the free surface of tested specimens.

5.2 Future Considerations

The work that has been conducted here will be used as a starting point for detailed investigations into the effects of stress wave propagation induced via laser loading. In particular three areas of interest have been determined for future investigations using the laser loading technique. The first is the investigation of blanket metallic multilayer systems of decreasing layer thickness subjected to laser loading; the second is the investigation of dynamic interfacial fracture of thin metallic films and silicon; the third is the use of digital image correlation and high speed imaging to capture the spallation process of thin films.

5.2.1 Metallic Multilayer Systems

As mentioned in the introduction, previous work conducted by Misra *et al.* (2005) has shown that as the layering thickness of multilayered materials decreases there is a significant

increase in their strength. It is believed that this strength increase is due to dislocation motion with in the layers and their interaction with the layer interfaces. To probe the dislocation interactions at micron and nanometer length scales alternating metallic layers can be deposited on a silicon substrate in succession creating a stack of many layers of thin films. Specimens of alternating layers of either copper and gold or copper and silver will be examined. Mr. K. Baldwin of Los Alamos National Laboratory (LANL) with the Center for Integrated Nanotechnologies has manufactured four sets of copper-gold multilayer samples on silicon substrates using magnetron sputtering. For a benchmark comparison, single layer 10 micron thick films, i.e., either only one copper layer or one gold layer will also be tested initially. Figure 5.1 shows schematics of metallic multilayer systems of increasing layer number but with the same total thickness of 10 μm.

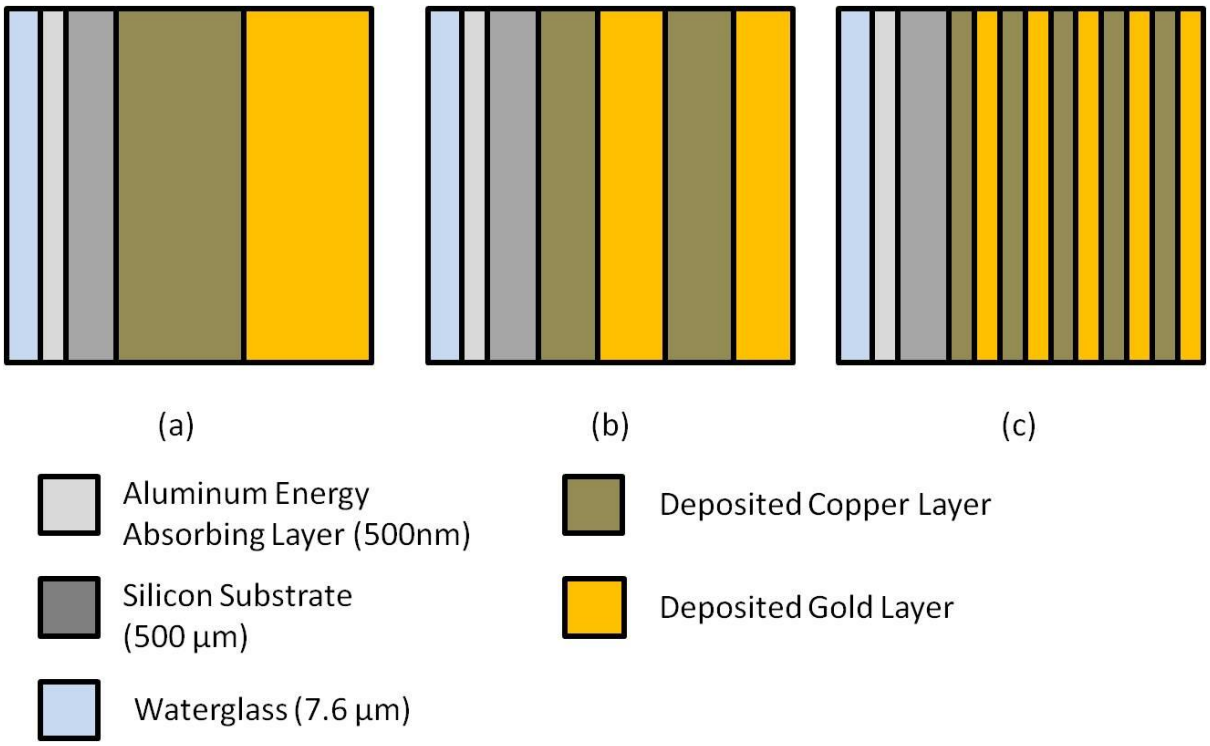

Figure 5.1: Copper-gold multilayer systems. (a) Specimen of two layers, (b) Specimen of four layers (c) Specimen of ten layers etc.

The response of the metallic multilayer systems to laser loading will be analyzed using *in situ* transmission electron microscopy (TEM) to determine the interaction of dislocations with material interfaces on loaded specimens. Additionally the metallic multilayer specimens will be able to provide insight into the interfacial strength between thin film metallic interfaces. This study will be accomplished by testing specimens at laser energy levels high enough to cause spallation or blistering of the metallic layers (see Figure 2.1). In tandem with this experimental study, a computational model will be constructed to mimic the multilayer material response to laser loading. The computational model developed will be physically based on dislocation interactions that are seen from the TEM study of loaded specimens, using stress wave inputs obtained from the study presented in this thesis.

5.2.2 Dynamic Fracture

Specimens that contain micro-voids, formed using microfabrication techniques, can also be tested using the laser loading method. Micro-void specimens will be manufactured using the following process: Silicon wafers will be patterned with photoresist, then selectively etched using an inductive coupled plasma machine to create micro features (typically circles) on silicon substrates. The wafers will then be bonded using high temperature fusion bonding to obtain a nearly perfect bonded interface between the silicon wafers resulting in a sample with an enclosed micro-void as shown (exaggerated) in Figure 5.2(a). Additionally samples of metallic layers with micro-voids can be created to determine the fracture toughness of metallic thin films, such as Au and Ag. A schematic of a micro-void metallic sample layup is shown in Figure 5.2(b). Through laser loading of the micro-void samples the voids can be induced to tensile failure by the reflected tensile release wave from the specimen free surface. Thus the dynamic facture toughness of the silicon and of metallic thin films under ultra-high loading rates can be determined experimentally.

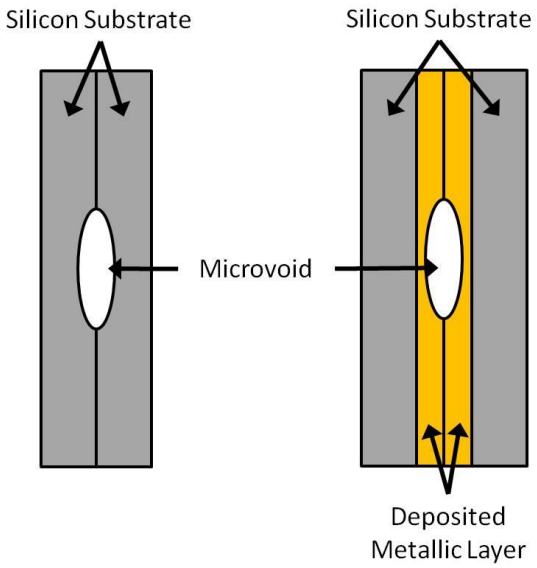

Figure 5.2: Micro-void specimen lay-up

5.2.3 High Speed Imaging of Deformation Induced by Laser Loading

The laser loading control illustrated in this work will allow us to perform experiments without necessarily having to measure the back face velocity in each case. Therefore this will allow for an alternative experimental investigation of the rear surface, such as high speed photography. Through the use of high speed imaging, the deformation process will be captured and can be compared against the determined stress wave profiles from this work to understand the point at which spallation begins.

References:

Anderholm, N. C. (1970). "Laser-Generated Stress Waves." Applied Physics Letters **16**(3): 113-115.

Dally, J. W. and W. F. Riley (2005). Experimental Stress Analysis. Knoxville, College House Enterprises, LLC.

Gupta V. and Argon, A., (1990). Measurement of Interface Strength by laser-pulse induced spallation, *Materials Science and Engineering*. A126 105-117.

Gupta, V. and Argon, et al. (1992). Measurement of interface strength by a laser spallation technique. Journal of the Mechanics and Physics of Solids, **40**(1): 141-180.

Gupta, V. and J. Yuan (1993). "Measurement of Interface Strength by the Modified Laser Spallation Technique. II. Applications to Metal/Cermaic Interfaces." Journal of Applied Physics **74**(4): 2397-2404.

Gupta, V. and J. Yuan, et al. (1993). "Nanosecond Rise-Time Stress Pulses Using Lasers for Applications to Material Characterization." Experimental Techniques in the Dynamics of Deformable Solids **165**: 61-72.

Kandula, S. S. V. (2008). Delamination of thin film patterns using laser-induced stress waves. Aerospace Engineering. Urbana-Champaign, University of Illinois. **Doctorate of Philosophy:** 115.

Kimberley, J. (2008). Failure of microelectromechanical systems under dynamic loading: an experimental and numerical investigation. Aerospace Engineering. Champaign-Urbana, Univeristy of Illinois. **Doctorate of Philosophy:** 189.

Kimberley, J., Chasiotis, I., and Lambros, J., (2008) . Failure of microelectromechanical systems subjected to impulse loads. International Journal of Solids and Structures, **45**: 497-512.

Kolsky, H. (1953). Stress Waves in Solids. Oxford, Oxford University Press.

Madou, M. J. (2002). Fundamentals of Microfabrication: The Science of Miniaturization. Boca Raton, CRC Press.

Misra, A., J. P. Hirth, et al. (2005). "Length-scale-dependent deformation mechanisms in incoherent metallic multilayered composites." Acta Materialia **53**: 4817-4824.

Pronin, A. N. and V. Gupta (1998). "Measurement of Thin Film Interface Toughness by Using Laser-Generated Stress Pulses." Journal of the Mechanics and Physics of Solids **46**(3): 389-409.

Skeen, C. H. and C. M. York (1968). "Laser-Induced "Blow-Off" Phenomena." Applied Physics Letters **12**(11): 369-371.

Wang, J., N. R. Sottos, et al. (2004). "Tensile and mixed-mode strength of a thin film-substrate interface under laser induced pulse loading." Journal of the Mechanics and Physics of Solids **52**: 999-1022.

Wang, J., Weaver, R.L., and Sottos, N.R., (2002). A parametric study of laser induced thin film spallation. Experimental Mechanics, **42**(1): 74-83.

White, R. M. (1963). "Generation of Elastic Waves by Transient Surface Heating." Journal of Applied Physics **34**(12): 3559-3567.

Yuan, J. and V. Gupta (1993). "Measurement of interface strength by the modified laser spallation technique. I. Experiment and simulation of the spallation process." Journal of Applied Physics **74**(4): 2388-2398.

Zukas, J.A., Nicholas, T., Swift, H.F., Grezczuk, L.B., and Curran, D.R., (1982). Impact Dynamics. New York: Wiley.